



Cobalt aluminate spinel-derived catalysts for glycerol aqueous phase reforming



A.J. Reynoso^a, J.L. Ayastuy^{a,*}, U. Iriarte-Velasco^b, M.A. Gutiérrez-Ortiz^a, Chemical Technologies for the Environmental Sustainability Group

^a Department of Chemical Engineering, Faculty of Science and Technology, University of the Basque Country UPV/EHU, Sarriena S/N, 48940 Leioa, Spain

^b Department of Chemical Engineering, Faculty of Pharmacy, University of the Basque Country UPV/EHU, Paseo de la Universidad, 7, 01006 Vitoria, Spain

ARTICLE INFO

Keywords:

Cobalt aluminate
Spinel
Aqueous phase reforming
Glycerol
Hydrogen

ABSTRACT

Catalytic activity at mild (235 °C/3.5 MPa) and severe (260 °C/5.0 MPa) APR conditions was investigated over catalysts based on cobalt aluminate spinel synthetized by coprecipitation. Co/Al ratio was varied and physicochemical characteristics were assessed by N₂ adsorption, H₂ chemisorption, XRD, H₂-TPR, DRS-UV, FTIR, CO₂-TPD, NH₃-TPD and XPS. Formation of cobalt aluminate produced strong Co-O-Al interaction in the catalyst precursor leading to improved Co dispersion upon activation. Co/Al ratio could be used to tune catalyst characteristics, thus selectivity towards the desired reaction pathway. Overall, Co/Al above the stoichiometric value produced smaller and more stable metallic Co, which allowed best APR performance. For instance, at 235 °C/3.5 MPa glycerol conversion and conversion to gas of 0.625CoAl (88% and 22%) were notably higher than those of bare Co₃O₄ (23% and 5%). At severe conditions, 0.625CoAl catalyst produced 231 μmol_{H2}/g_{cat} min (60% H₂). Statistical analysis of data collected from long-term run was used to investigate reaction mechanism. Long-term run revealed that sintering and oxidation were main mechanisms for catalyst deactivation whereas some leaching of Co nanoparticles, and carbonaceous deposition was also detected.

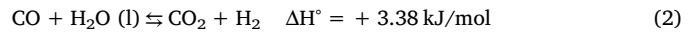
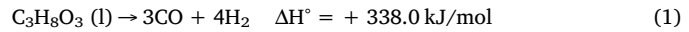
1. Introduction

The mitigation of the global warming has been the main driving force of the current research and development of hydrogen-based energy systems, more environmentally advantageous and efficient than fossil fuels. Hydrogen can be produced from various feedstocks, among them, the biomass-derived feedstocks are carbon neutral, since the CO₂ produced in the process is consumed for the biomass growth [1]. The huge increase in the worldwide production of biodiesel, a biomass-derived fuel [2] leads to large amount of surplus glycerol (about 10 wt.% of the produced biodiesel), which must be converted into higher value-added chemicals to guarantee the economic viability of biodiesel industries. The highly functionalized glycerol molecule makes it prone to different processes such as oxidation, hydrogenolysis or dehydration [3]. Also, it can be used to produce fuels such as hydrogen by catalytic steam reforming (SR), pyrolysis and gasification [4–7]. However, these processes involve high temperatures and many side reactions, which decrease hydrogen selectivity [4].

Aqueous-phase reforming (APR) of biomass-derived oxygenated compounds for H₂ production [8] represents several advantages in

comparison to SR, such as lower energy demand and lower operation temperature. The later makes APR thermodynamically more favorable towards the formation of hydrogen with low CO content, due to the Water-Gas Shift (WGS) equilibrium, water reacting from liquid phase [9]. In addition, the undesirable decomposition reactions and deactivation by coke are minimized. APR of biomass-derived oxygenated compounds is typically carried out at moderate temperature (200–260 °C) and elevated pressure (2–5 MPa), the later necessary to keep the reactants in the liquid phase.

The glycerol APR involves, ideally, the following two parallel reactions, which produce hydrogen:



The overall APR reaction is the sum of Reactions (1) and (2):



In the ideal glycerol APR, 7 mol of hydrogen are obtained from each mole of reacted glycerol, together with 3 mol of CO₂. However, a number of parallel reactions can also occur, such as CO and CO₂

* Corresponding author.

E-mail address: joseluis.ayastuy@ehu.eus (J.L. Ayastuy).

methanation, Fischer-Tropsch or hydrogenations, which are undesirable because hydrogen is consumed. Dehydration reactions are also detrimental, because the subsequent hydrogenation to alkanes decreases selectivity to hydrogen [10].

An active catalysts for the APR must have high catalytic activity for C–C and C–H bonds cleavage and WGS reaction, and inhibit C–O bond cleavage, Fisher-Tropsch and methanation reactions [11]. High H₂ and CO₂ yields are favored by the C–C and C–H bonds cleavage, which occur in the metallic sites of the catalysts. The C–O scission, which occur in the acid sites, leads to alkane production [12]. Therefore, tuning the catalysts metallic and acid properties, the APR process could be ideally focused to hydrogen or to alkanes production.

Supported Pt catalysts have emerged as benchmark catalyst for hydrogen production by APR of oxygenated hydrocarbons. Pt has been extensively investigated as either monometallic [13–18] or bimetallic [19–25] catalytic system. However, due to the high cost of Pt, more cost-effective metals are seek [26–28]. Cobalt is characterized by a high C–C bond cleavage [29] and WGS activity [30] and has been reported as a good choice for steam reforming [31–37]. It is scarce, however, the number of studies carried out concerning APR of oxygenated hydrocarbons with cobalt-based catalysts [38–40]. The main drawbacks of cobalt based catalysts in liquid phase reactions are related to the oxidation and leaching of metal phase [41]. As a result, rapid deactivation of the catalysts can occur [40]. In addition, conventional supports such as γ -alumina show low stability under APR hydrothermal conditions, as it transforms through hydration into more acidic bohemite (AlOOH) phase, leading to catalyst deactivation [42].

Based on the above aspects, we hypothesize that cobalt aluminate, a transition metal spinel, could be a promising alternative as precursor of cobalt-based catalyst, which conjugates the catalytic advantages of a highly active metal supported onto a stable structure. Mesoporous cobalt aluminate spinel (CoAl₂O₄) has low surface acidity, high thermal and pH stability [43]. After reduction at high temperature metal particles can be rearranged within the aluminate matrix with a relatively high dispersion of metal crystallites in the surface [44]. So far, cobalt aluminates have been studied for methane dry reforming [45], methanol SR [46] or propane dehydrogenation [47]. Catalysts obtained from cobalt aluminate precursors have shown good stability in methane dry reforming [45] and alkane dehydrogenation. To the best of our knowledge, glycerol APR with cobalt aluminate catalysts has not been yet investigated.

In the present work, cobalt aluminate spinels were synthesized by coprecipitation. The effect of the Co/Al atomic ratio on the physico-chemical characteristics was investigated by a wide number of techniques such as N₂ adsorption/desorption, XRD, H₂-TPR, H₂-chemisorption, FTIR, DRS UV-vis-NIR, XPS, NH₃-TPD and Raman. Catalytic performance in the glycerol APR was evaluated in a continuous up-flow plug reactor.

2. Experimental

2.1. Catalysts preparation

Spinel-type cobalt aluminates (with Co/Al molar ratio 0.25, 0.5 and 0.625) and bare Co₃O₄ were prepared as follows: a proper amount of an aqueous solution of Co(NO₃)₂·6H₂O (99.999% trace metal basis, Sigma Aldrich) and Al(NO₃)₃·9H₂O (98% trace metal basis, Fluka) was added dropwise into a beaker containing an aqueous solution of Na₂CO₃ under stirring, for around 2 h, at room temperature at constant pH 10, adjusted with NaOH solution (2 M). The resulting suspension was aged at room temperature for 24 h, filtered, washed several times with de-ionized water and dried at 110 °C for 17 h. The solid was ground to fine powders and then calcined in a muffle furnace at 500 °C (heating rate 5 °C/min) for 5 h in a static air atmosphere. During calcination, the maximum temperature in the solid did not surpass 505 °C. The as-prepared solids were denoted as XCoAl, where X is the nominal Co/Al

molar ratio. For comparative purposes, γ -Al₂O₃ was also prepared by simple calcination in air (at 500 °C) of aluminium nitrate. Commercial CoO (Sigma Aldrich) was also used as reference. Reduction of samples (ex situ) was carried out in a quartz reactor at 600 °C for 2 h (heating rate 5 °C/min) in 50% H₂-He flow (50 mL/min).

2.2. Characterization techniques

Bulk composition of the samples was measured by inductively coupled plasma atomic emission spectroscopy (ICP-AES). Textural properties of the solids were obtained from the nitrogen adsorption-desorption isotherms determined at 77 K in a Micromeritics TRISTAR II 3020 equipment. Prior to the adsorption, the samples were outgassed at 300 °C for 10 h. The specific surface area and the main pore size were determined with the BET and BJH methods, respectively.

The reduction behavior was studied by hydrogen temperature-programmed reduction (H₂-TPR) in a Micromeritics AutoChem 2920 apparatus. About 50 mg of the calcined sample was initially flushed in He stream at 500 °C for 1 h (heating rate 10 °C/min) and then cooled to room temperature in Ar. Then, a 5% H₂-Ar flow was passed through the bed containing the sample while temperature was increased up to 950 °C (heating rate 10 °C/min) and hold for 1 h. The H₂ consumption rate was monitored in a thermal conductivity detector (TCD).

The exposed cobalt surface area was determined by H₂ pulse chemisorption in a Micromeritics AutoChem 2920 apparatus. The sample was reduced at 600 °C for 30 min under 5% H₂-Ar flow and cooled down to 35 °C under Ar flow. Then, H₂ pulses (loop volume 0.5312 mL) were injected until the eluted peak area of consecutive pulses remained constant. The number of exposed Co atoms was calculated from the volume of H₂ chemisorbed by assuming a H/Co stoichiometry of 1/1 [48] and a cross-sectional area of 0.0662 nm² per Co atom [49].

The identification of crystalline phases and the morphological study was carried out by powder XRD. The XRD diffractograms were obtained on a PANalytical X'pert PRO diffractometer with Cu K α radiation ($\lambda = 1.5406 \text{ \AA}$) and graphite monochromator. Each sample was scanned from 10 to 80° (20), with a step size of 0.026° (20) and a counting time of 2 s. Phase identification was conducted by comparison with JCPDS database cards. Lattice parameters were calculated by Fullprof software. The crystallite average size of each species was calculated from its most intense peak broadening applying the Scherrer equation.

The speciation of cobalt cations (coordination and oxidation states) was determined by Diffuse Reflectance UV-vis NIR spectroscopy (DRS UV-vis NIR) in a Cary 5000 equipment coupled to Diffuse Reflectance Internal 2500 within a range of 200–2500 nm. The reflectance data were converted into absorption by the Kubelka-Munk transformation. Fourier transform infrared spectroscopy (FTIR) transmittance spectra were recorded in the 400–4000 cm⁻¹ range in a Cary 600 Series FTIR apparatus by employing KBr pellet technique.

The total acidity/basicity of the reduced samples was evaluated by means of pulse NH₃/CO₂ adsorption followed by subsequent temperature programmed desorption (TPD) of NH₃/CO₂, respectively. Experiments were carried out in a Micromeritics AutoChem 2920 equipment coupled to Mass Spectroscopy (MKS, Cirrus 3000). Each sample was initially pretreated in a He stream at 550 °C for 1 h (heating rate 10 °C/min) and cooled down to room temperature. Then, it was reduced at 600 °C in 5% H₂-Ar flow (heating rate 10 °C/min), hold for 2 h and cooled down in helium flow (to 90 °C for NH₃ adsorption and to 40 °C for CO₂ adsorption). For acidity measurements, a series of 10% NH₃-He pulses were introduced at 90 °C. For basicity measurements a series of 5% CO₂-He pulses were introduced at 40 °C. Subsequently, the sample was exposed to He flow for 60 min at the corresponding temperature of adsorption stage in order to remove reversibly and physically bound NH₃/CO₂ from the surface. Finally, the temperature was raised to 950 °C (heating rate 5 °C/min) and the resultant signal was followed by MS (*m/z* = 17 and 44, for NH₃ and CO₂, respectively). The

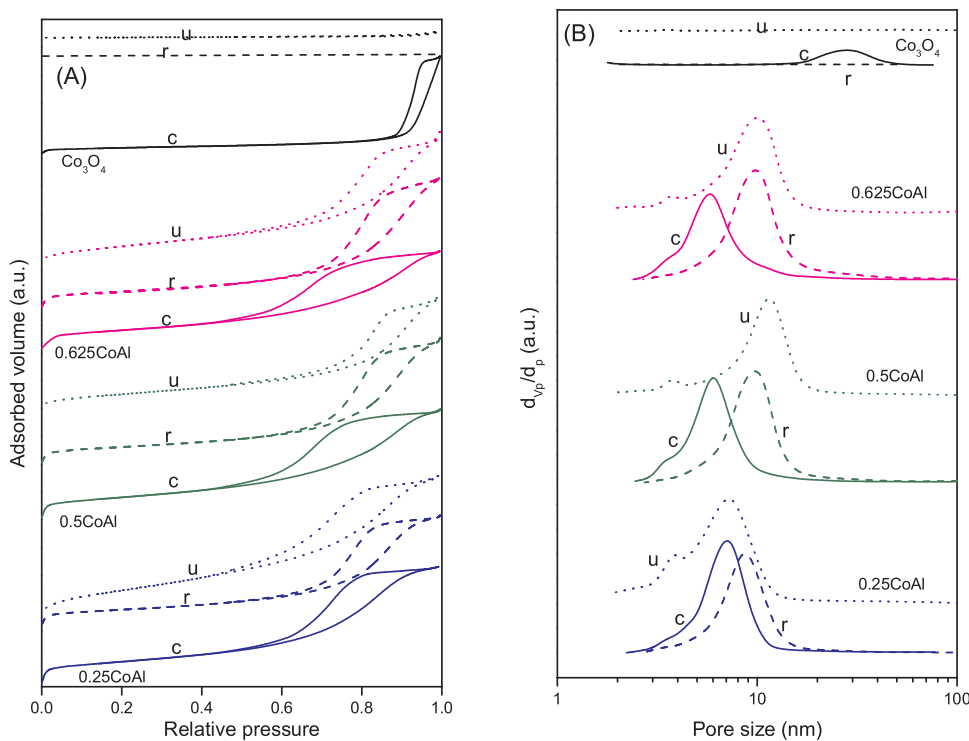


Fig. 1. Nitrogen adsorption-desorption isotherms (A) and pore size distribution (B) of the calcined (c, solid lines), reduced (r, dashed lines) and used (u, dotted lines) samples.

total acidity and basicity of the samples was calculated from the integration of the pulses, and the strength of the acid and basic sites was evaluated from the corresponding TPD curves.

X-ray photoelectron spectroscopy (XPS) was used to detect the electronic state of Co and Al in the prepared samples. The spectra were measured using a SPECS spectrometer with Phoibos 150 1DDLD analyzer and monochromatized Al K α (1486.7 eV) X-ray radiation in ultrahigh vacuum. The binding energies were calibrated by taking C 1s peak (284.6 eV) of adventitious carbon as reference. The peaks were deconvoluted after background subtraction, using a mixed Gaussian-Lorentzian function.

Raman analysis of the spent catalysts was carried out in a Renishaw InVia Raman spectrometer, joined to a Leica DMLM microscope, using a laser of 514 nm (ion-argon laser, Modu-Laser). The power of the laser was reduced in order to avoid the photo-decomposition of the samples by using neutral density filters. In order to improve the signal to noise ratio, 40 s were used for each spectrum and 10 scans were accumulated at 10% of the maximum power of the 514 nm laser, in the 100 cm⁻¹ to 1800 cm⁻¹ spectral window.

2.3. Catalytic performance

A bench-scale fixed-bed up-flow reactor (Microactivity Effi, PID Eng & Tech), with an internal diameter of 5.1 mm and a height of 305 mm was used. In a typical catalytic test, about 0.5 g of catalyst (particle size 0.04–0.16 mm) was placed on a stainless steel frit and covered with a quartz wool plug, giving a bed volume of 0.6 cm³. Before the reaction, the catalyst was reduced *in situ* under 10%H₂/He flow at 600 °C for 1 h (heating rate 10 °C/min) at atmospheric pressure. When the desired pressure was reached, the He was switched to bypass and 0.2 ml/min of a 10 wt.% glycerol aqueous solution was pumped into the reactor while the temperature was raised at 5 °C/min. Two temperatures were tested, 235 °C/3.5 MPa and 260 °C/5.0 MPa at a Weight Hourly Space Velocity (WHSV) of 24.5 h⁻¹ (determined as the ratio between feed mass-flowrate and mass of fresh catalyst). The reaction products were cooled down to 5 °C by the Peltier cell and the two phases separated. The non-

condensed gas was online analyzed by a gas chromatograph (μGC Agilent) equipped with four parallel columns (Al₂O₃-KCl 10 m, PPQ 10 m, MS5A 10 m, He as carrier, and MS5A 10 m, Ar as carrier), while the liquid products were collected every 30 min and analyzed by either off-line gas chromatograph (GC-MS Agilent, CP-Wax 5CB column) or HPLC (Waters 616, Hi-Plex H column) equipped with Refraction Index Detector. The total organic carbon (TOC) was measured off-line on a Shimadzu TOC-5050A apparatus. The carbon balance was above 97% for all the experiments.

The total glycerol conversion (X_{Gly}) was calculated on the basis of glycerol molar flow, as follows:

$$X_{\text{Gly}} (\%) = 100 \times \frac{F_{\text{Glycerol}}^{\text{in}} - F_{\text{Glycerol}}^{\text{out}}}{F_{\text{Glycerol}}^{\text{in}}} \quad (4)$$

The carbon conversion to gas (X_{gas}) was calculated on the basis of carbon atoms molar flow, as follows:

$$X_{\text{Gas}} (\%) = 100 \times \frac{F_{\text{Catoms}}^{\text{in}} - F_{\text{Catoms,liquid}}^{\text{out}}}{F_{\text{Catoms}}^{\text{in}}} \quad (5)$$

Selectivity to gas (S_{gas}) was defined as the fraction of carbon moles converted into gas phase per converted glycerol moles:

$$S_{\text{gas}} (\%) = 100 \times \frac{F_{\text{Catoms}}^{\text{in}} - F_{\text{Catoms,liquid}}^{\text{out}}}{F_{\text{Gly}}^{\text{in}} - F_{\text{Gly}}^{\text{out}}} \times \frac{1}{3} \quad (6)$$

Hydrogen selectivity (S_{H_2}) was defined as the ratio between the moles of hydrogen produced and moles of glycerol reacted, multiplied by 1/7 (inverse of the reforming glycerol:hydrogen ratio, according to Reaction (3)):

$$S_{\text{H}_2} (\%) = 100 \times \frac{F_{\text{H}_2}^{\text{out}}}{F_{\text{Glycerol}}^{\text{in}} - F_{\text{Glycerol}}^{\text{out}}} \times \frac{1}{7} \quad (7)$$

The selectivity of the C-containing gas phase product i was calculated as follows:

Table 1

Textural and surface properties of the investigated catalysts.

Sample	Co/Al ^a (at./at.)	S _{BET} (m ² /g)			Surface acid sites density (μmol _{NH3} /m ²)	Surface basic sites density (μmol _{CO2} /m ²)	Number of exposed Co atoms (atoms/g) ^b		Leached metals (wt.%) ^c	
		calcined	reduced	spent			reduced	spent	Al	Co
0.25CoAl	0.267	136.2	96.6	284.4	0.78	2.20	2.28 × 10 ¹⁸	4.08 × 10 ¹⁷	2.2	2.1
0.5CoAl	0.498	132.3	102.8	172.6	0.60	1.95	3.92 × 10 ¹⁸	7.71 × 10 ¹⁷	13.7	3.2
0.625CoAl	0.634	125.3	101.7	178.2	0.51	1.90	23.0 × 10 ¹⁸	9.92 × 10 ¹⁷	1.5	1.6
Co ₃ O ₄	∞	37.7	7.36	5.8	0.06	2.01	1.22 × 10 ¹⁸	9.4 × 10 ¹⁷	–	0.3

^a From ICP-AAS.^b From H₂ chemisorption (H:Co = 1:1).^c From ICP-AAS in the condensable products at the end of run expressed as percentage of the amount of metal present in the parent catalyst.

$$S_i(\%) = 100 \times \frac{F_i^{out}}{F_{Glycerol}^{in} - F_{Glycerol}^{out}} \times \frac{C_{atoms,i}}{3} \quad (8)$$

Finally, hydrogen yield (Y_{H2}) was defined as the ratio between the moles of hydrogen produced and moles of glycerol fed to the reactor, multiplied by the stoichiometric factor 1/7:

$$Y_{H2}(\%) = 100 \times \frac{F_{H2}^{out}}{F_{Glycerol}^{in}} \times \frac{1}{7} \quad (9)$$

3. Results and discussion

3.1. Materials characterization

3.1.1. Chemical composition and textural properties

Fig. 1A and B shows the nitrogen adsorption-desorption isotherms and pore size distribution for the calcined (solid lines) and reduced (dashed lines) samples. Textural properties are detailed in Tables 1 and S1 (Supporting information). The experimental Co/Al atomic ratio was very close to the nominal value for all the samples.

The calcined samples, irrespective of Co/Al, showed type IV isotherms characteristic of mesoporous solids (IUPAC classification) and H2 type hysteresis loop at high relative pressures, characteristic of disordered porous materials. Micropore volume was negligible (t-plot method) indicating that only mesopores were developed in the prepared samples. The specific surface area (S_{BET}) of the binary XCoAl oxides was markedly larger than Co₃O₄ and moderately larger than γ-Al₂O₃ (117.9 m²/g). This was due to the mutual protective effect, that is, the presence of one oxide hinders the crystallization of the other, preventing the formation of large particles. It has been reported that the incorporation of aluminium can hinder the crystallization of the Co₃O₄, and vice versa, preventing the formation of large particles [50]. This phenomenon was more marked as Al loading increased (Co/Al decrease), as deduced from the S_{BET} increase from 125.3 m²/g for 0.625CoAl to 136.2 m²/g for 0.25CoAl (9% increase), as reported by others [51]. Accordingly, pore volume increased and pore size decreased with Al doping (see Table S1, Supporting information).

The corresponding pore size distribution curves, obtained from the adsorption branches (Fig. 1B), displayed a similar unimodal distribution for all aluminium-containing samples, with peaks centered at around 6.5 nm. On the other hand, Co₃O₄ had a much broader distribution, with an average pore diameter of 27.7 nm.

Reduced XCoAl samples displayed type IV isotherms and a combination of H1-H2 type hysteresis (Fig. 1A). As shown in Fig. 1B, after reduction, the pore size distribution shifted to larger values (around 70% increase) and, consequently, S_{BET} declined up to 30% (for 0.25CoAl), caused by the migration of the metallic cobalt from the CoAl₂O₄ lattice to the surface [52] and the dilution effect [53]. Interestingly, similar S_{BET} values were measured for all the reduced samples (96.6–102.8 m²/g range), that is, samples with higher amount of cobalt suffered the lesser S_{BET} decrease, suggesting that cobalt ions could have

stabilized the structure.

3.1.2. Metallic surface area and H₂-TPR

As could be expected, the number of exposed metallic cobalt atoms increased with the Co/Al ratio (Table 1). Upon reduction, cobalt atoms diffused towards the crystal surface agglomerating on the solid surface. It is noteworthy, however, that the exposed atoms exponentially increased with cobalt content of binary oxides, and a ten-fold increase was observed from sample 0.25CoAl to 0.625CoAl (2.28 × 10¹⁸–23.0 × 10¹⁸ Co atoms per gram, respectively). Contrarily, bare Co₃O₄ showed the least exposed cobalt atoms, as a consequence of sintering (see XRD data).

The H₂-TPR profiles are shown in Fig. 2A. γ-Al₂O₃ had no H₂ consumption in all the analysed temperature range (not shown). CoO exhibited a relatively broad reduction signal in the 250 °C–750 °C range, with two peaks, first at 400 °C and a second intense and broad peak at 610 °C [54]. Hydrogen consumption (13.5 mmol_{H2}/g) was slightly above the stoichiometric value (13.3 mmol_{H2}/g), what could be ascribed to the complete reduction of Co²⁺ ions to metallic Co and the coexistence of trace amounts of fully oxidized cobalt species on the surface of CoO, as also observed by FTIR (discussed below).

The reduction profile of Co₃O₄ shows two well defined peaks, the low temperature peak at 300 °C, related to the reduction of surface Co³⁺ to Co²⁺, and the second broad peak, at higher temperatures (maxima at about 425 °C), attributed to the reduction of Co²⁺ species to metallic cobalt [55]. For stoichiometric Co₃O₄, the ratio between the low and high temperature peak is 0.33. Experimentally, a ratio of 0.37 was measured for sample Co₃O₄. This corresponds to a bulk Co²⁺/Co³⁺ molar ratio of 0.35, somewhat lower than the stoichiometric value (Co²⁺/Co³⁺ = 0.5), which indicates its relative enrichment in Co₂O₃ (42% excess) in detriment of CoO. This would explain its higher than stoichiometric (16.6 mmol/g) hydrogen consumption.

H₂-TPR of Co/alumina calcined at 500 °C (prepared by wet impregnation at Co/Al = 0.5) was carried out for comparison purposes. The low temperature peak (355 °C) was attributed to Co³⁺ → Co²⁺ while the Co²⁺ → Co° reduction stage showed the contribution of three peaks (at 474 °C, 585 °C and 670 °C) depending on the interaction with the support. It is noteworthy that no CoAl₂O₄ was formed in this sample, although it was detected after calcination at 800 °C (Fig. S2, Supporting information). This suggests that the counter diffusion of Co and Al ions, necessary to form cobalt aluminate, was promoted by the calcination temperature.

The reduction of all the XCoAl samples started at around 135 °C and showed four peaks. The two low temperature peaks, at around 300 and 400 °C (peak I and II), were ascribed to the reduction of Co³⁺ to Co²⁺. The former was related to the surface cobalt cations without any interaction with the alumina or cobalt aluminate phase. Kung et al. [56] found that Al³⁺ ions polarize the Co–O bonds in the spinel-like mixed oxide thus increasing its reduction temperature. Therefore, it could be reasonably assumed that peak II corresponded to the reduction of Co³⁺ species in close interaction with alumina or cobalt aluminate. The

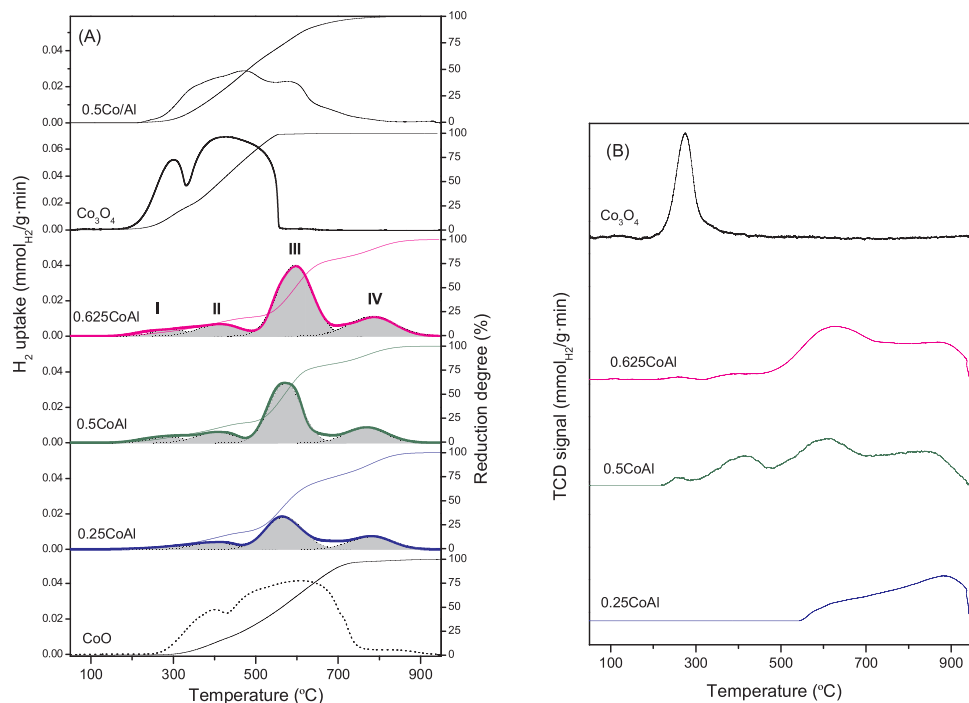


Fig. 2. H₂-TPR profiles of (A) fresh samples and (B) samples used in APR reaction.

reduction peak at around 580 °C (peak III) was assigned to Co²⁺ → Co°.

Peak IV was assigned to the reduction of cobalt ions in the cobalt aluminate (CoAl₂O₄) phase [57]. In order to confirm the assignment, the stoichiometric sample (0.5CoAl) was calcined at 800 °C and submitted to H₂-TPR analysis (Fig. S1A, Supporting information). Calcination at 800 °C notably decreased the hydrogen consumption at below 600 °C whereas it was increased at high temperature (peak IV). Indeed, formation of CoAl₂O₄ phase is favored at high calcination temperature [58], thus it could be reasonably assumed that peak IV reflects the reduction of cobalt in the cobalt aluminate phase.

It is interesting to note that peak III was significantly shifted to higher temperatures in the XCoAl samples (by about 150 °C) as compared with bare Co₃O₄. The interaction between the cobalt ions and the support (mixture of alumina and cobalt aluminate) notably hindered both reduction steps, Co³⁺ to Co²⁺ and Co²⁺ to Co°. The later occurred at the highest temperature for catalyst 0.625CoAl. Indeed, this strong Co-support interaction probably led to an elevated Co dispersion (Table 1) and might be attributed to the high cobalt aluminate content of this sample. Co/alumina samples prepared by wet impregnation contained more free cobalt (peak I) than those prepared by coprecipitation.

In general, the formation of free Co₃O₄ and cobalt aluminate phase

increased with Co loading (Table 2). For instance, weight percent of Co₃O₄ accounted for 16.4% in 0.25CoAl and reached up to 34.2% for catalyst 0.625CoAl, while CoAl₂O₄ increased from 19.3% to 24.1%, respectively. However, the fraction of cobalt that was incorporated to the alumina matrix to form cobalt aluminate followed the opposite trend. As a result, the Co mole ratio as CoAl₂O₄ to Co₃O₄ significantly decreased from 1.6 to 0.96 with increasing Co/Al. Note that regardless of the Co/Al ratio, the fraction of easily reducible Co₃O₄ particles at the surface remained constant (around 6%), as inferred from similar contribution of peak I to total hydrogen consumption.

Based on the H₂-TPR results, XCoAl catalysts were reduced at 600 °C for 1 h prior to catalytic runs. It was confirmed (see Fig. S1B, Supporting information) that all Co₃O₄ in samples was completely reduced, and also around 10% of the cobalt aluminate spinel phase.

The overall Co/Al atomic ratio was calculated from Co 2p to Al 2p peak intensities (Table S2, Fig. S5, Supporting information). In line with the above results, the ratio between Co and Al atoms was lower in surface than in the bulk. This surface enrichment on Al³⁺ ions was attributed to the lower surface free energy of Al as compared to Co [59]. It is interesting to note, however, that the surface Co/Al increased in parallel to bulk Co/Al. TPR data amounted to around 6% of the cobalt loaded that existed as surface Co⁸⁸⁺ species in all the prepared XCoAl samples.

Table 2
Results from H₂-TPR studies of the XCoAl samples.

Sample	H ₂ uptake (mmol _{H2} /g)					Bulk composition ^a		Co distribution ^b	H ₂ uptake(mmol _{H2} /g)
	Total	Peak I	Peak II	Peak III	Peak IV	Co ₃ O ₄	CoAl ₂ O ₄		
0.25CoAl	3.81	0.190 (291)	0.492 (398)	2.038 (570)	1.090 (780)	0.164	0.193	1.60	3.19
0.5CoAl	5.73	0.348 (297)	0.723 (403)	3.484 (572)	1.175 (766)	0.274	0.208	1.03	4.90
0.625CoAl	7.04	0.392 (292)	0.881 (413)	4.407 (594)	1.360 (783)	0.342	0.241	0.96	4.98
Co ₃ O ₄	17.40	4.70 (300)	12.70 (425)	0	0	1.0	0	0	1.81

In parenthesis the temperature of the peak (in °C).

^a Weight fraction in catalyst as Co₃O₄ or CoAl₂O₄ (from H₂-TPR).

^b Co distribution as bulk CoAl₂O₄/Co₃O₄ mole ratio (from H₂-TPR).

^c Total hydrogen consumption of spent catalyst.

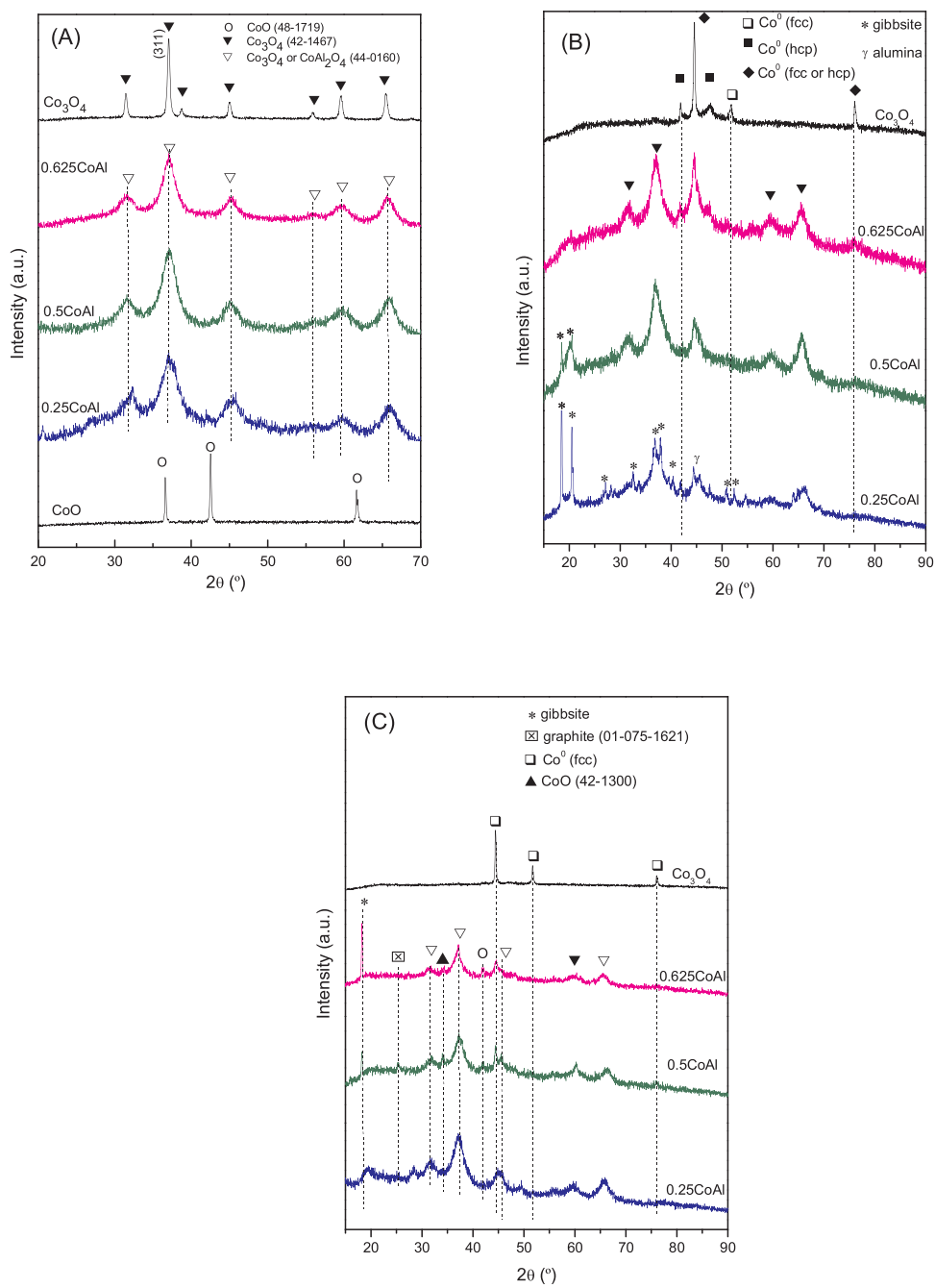


Fig. 3. XRD patterns of (A) calcined samples, (B) reduced samples and (C) used catalysts.

3.1.3. XRD analysis

All the diffraction peaks of calcined samples (Fig. 3A) matched with the reference cobalt aluminate (PDF 00-044-0160) and cobalt oxide (PDF 00-042-1467) spinel. It should be noted that both Co_3O_4 and CoAl_2O_4 crystallize in the same $Fd\text{-}3m$ spatial group and cubic system, which makes difficult to distinguish between both phases by XRD technique (the peaks were ascribed to either Co_3O_4 or CoAl_2O_4 , Fig. 3A). Characteristic peaks of CoO and Co_2O_3 were not observed in sample Co_3O_4 . $\text{H}_2\text{-TPR}$ data suggested these could be formed, thus, it is likely they formed as small crystals (below detection limit 2–5 nm) or amorphous phase.

As deduced from data in Table 3, the size of CoAl_2O_4 nanocrystals increased with Co/Al. Also, lattice parameter (a) clearly shifted towards higher values, thereby suggesting a progressive formation of CoAl_2O_4 . The incorporation of Co^{2+} ions to the CoAl_2O_4 lattice brought about its

Table 3
Results from XRD studies of the calcined and reduced samples.

Sample	Calcined samples		Reduced samples			$d_{\text{Co}(fcc)}$ (nm)
	d_{spinel} (nm)	a_{spinel} (nm)	$d_{\text{Co}(hcp)}$ (nm)	$d_{\text{Co}(fcc)}$ (nm)	$d_{\text{Co}(both)}$ (nm)	
0.25CoAl	3.8	0.7993 ± 0.00584	21.0	n.d.	n.d.	n.d.
0.5CoAl	4.1	0.8031 ± 0.00081	27.6	n.d.	18.2	34.4
0.625CoAl	5.0	0.8040 ± 0.00135	22.8	11.6	16.5	25.7
Co_3O_4	19.7	0.8059 ± 0.00086	36.4	20.1	28.3	43.0

expansion due to the difference in the ionic radii between Co^{2+} (0.74 Å) and Al^{3+} (0.53 Å) [59]. Also, it seems interesting to note that Co_3O_4 sample showed smaller lattice parameter (0.8059 nm) than that of pure cobalt oxide (0.80837 nm, PDF 00-042-1467), which supports

our sample is non-stoichiometric cobalt oxide, as previously deduced from its reduction behavior.

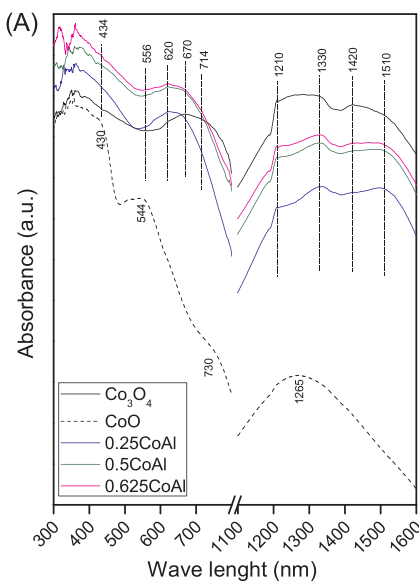
Reduced Co_3O_4 showed no diffraction peaks related to oxidized cobalt species (Co_2O_3 , Co_3O_4 and CoO), what implies that all cobalt was reduced, in line with H₂-TPR. Instead, diffraction lines of metallic cobalt (Co°) were clearly visible, either in face-centered cubic (*fcc*) (51.8°, PDF 00-015-0806) or hexagonal closed packed phase (*hcp*) (41.8°, 47.6°, PDF 00-005-0727). Simultaneous presence of both phases was confirmed at the highest Co/Al ratio (0.625CoAl). However, only *hcp* Co° was identified in the rest of reduced samples. It has been reported that *hcp* Co° crystallites are stable at above 40 nm. However, smaller *fcc* metallic cobalt crystallites were measured, what suggests that mixed phases of *hcp* and *fcc* could be present in our catalysts. It has been reported that *hcp* to *fcc* phase transition of metallic cobalt can occur upon reduction above 400 °C [60].

The occurrence of various diffraction peaks at low Co/Al could be ascribed to gibbsite (PDF 033-0018) and γ -alumina (PDF 01-079-1558). Indeed, water vapor is released during the reduction of cobalt oxide which may partially hydrate the $\gamma\text{-Al}_2\text{O}_3$ to gibbsite at high aluminium loading (i.e. high $\gamma\text{-Al}_2\text{O}_3$ content) [61].

It is noteworthy to point out the notably smaller Co° particle size obtained after reduction of XCoAl precursors (around 40–60% smaller). Indeed, Co/Al ratio could be used to tune the Co_3O_4 to CoAl_2O_4 ratio (see Table 2), and therefore, the environment in which cobalt species are reduced. Our results suggest that the strong interaction between Co species and the support in the prepared XCoAl catalysts can effectively improve dispersion of the metallic active phase upon catalysts activation [62]. Growth of the metallic Co nanoparticles, as compared to the parent calcined spinel was observed, as due to the coalescence in the surface of cobalt particles migrated from the bulk.

3.1.4. DRS UV-vis NIR analysis

Fig. 4A shows the UV-vis-NIR spectra of the prepared catalyst and CoO , used as reference. The spectrum of CoO consisted of two absorption maxima centered at 1265 and 544 nm, with a shoulder at 730 nm. The strong absorption band at 430 nm can be attributed to metal to ligand charge transfers. Accordingly, these bands were assigned to Co^{2+} ions in octahedral (Oh) coordination [63]. Co_3O_4 crystallizes in the cubic normal spinel structure with Co^{2+} ions occupying tetrahedral (Td) coordination while the Co^{3+} ions hosted an octahedral surrounding. The observed broad absorption band at 670 nm was attributed to $\nu_2(^4\text{A}_2 \rightarrow ^4\text{T}_1(\text{P}))$ transition of tetrahedral Co^{2+} .



Additional evidence concerning the presence of the latter comes from a set of bands in the NIR region (1200–1500 nm) which are characteristics of the $\nu_1(^4\text{A}_2 \rightarrow ^4\text{T}_1(\text{F}))$ transition [63] (not shown). Characteristic bands of octahedral Co^{3+} ions are more difficult to distinguish. According to crystal-field theory Co^{3+} (Oh) shows two bands, at 714 nm and at 434 nm, of comparable intensity associated with $\nu_1(^1\text{A}_1 \rightarrow ^1\text{T}_{1g})$ and $\nu_2(^1\text{A}_1 \rightarrow ^1\text{T}_{2g})$, respectively. The presence of octahedral Co^{3+} ions could be deduced from the presence of the broad band, described above, which enclosed the bands of the two Co species (Co^{2+} (Td) and Co^{3+} (Oh)).

The spectra of the calcined XCoAl samples was very similar to Co_3O_4 . It is interesting to note from **Fig. 4A** that an appreciable blue-shift is noticed in the tetrahedrally coordinated Co^{2+} ions charge transfer transitions (from 670 nm to 556 and 620 nm) and ascribed to the interaction of such ions with alumina [64]. Two features can be noted at increasing Al content (decreasing Co/Al): (i) The intensity ratio of bands at 1330 to 1210 nm increased, and (ii) the ratio 1420 to 1501 nm decreased. Both features could be assigned to the increase in the Co-Al interaction.

A more careful analysis of the UV-vis DRS spectra of the calcined XCoAl samples evidenced that the relative intensity of transitions bands in the UV-vis region with respect to NIR bands decreased with Co/Al ratio. According to [65] tetrahedral cobalt structure (which lacks center of symmetry) exhibits stronger absorption in NIR region than the octahedral cobalt structure (with center of symmetry). These results indicate an increase in the amount of tetrahedral Co^{2+} sites with Co/Al, in line with previously shown TPR data.

The DRS UV-vis NIR spectra of reduced samples (**Fig. 4B**) confirmed the existence of metallic Co (characteristic absorption band at 274 nm) and the absence of any Co^{88+} ionic species (characteristic absorption bands above 300 nm) on Co_3O_4 catalyst surface. The later species were, however, evident in reduced XCoAl samples, in agreement with XRD. In the visible region, all samples showed the characteristic triplet of Co (Td), though, much less intense than for the calcined counterparts. Additionally, a new band, ascribed to Co^{3+} (Oh), arose at 750 nm [66]. It is interesting to note that the intensity of NIR region bands corresponding to Co in tetrahedral structure decreased considerable for the reduced samples. This could reflect that the tetrahedral coordination is more easily reducible [67].

3.1.5. FTIR analysis

The FTIR spectra of calcined samples are shown in **Fig. 5**. The

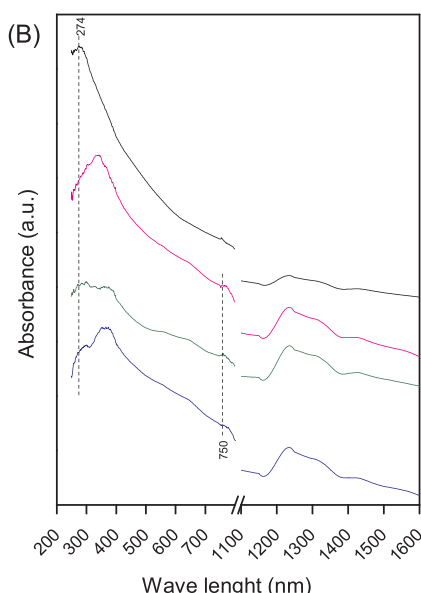


Fig. 4. DRS spectra of (A) calcined samples and (B) reduced samples.

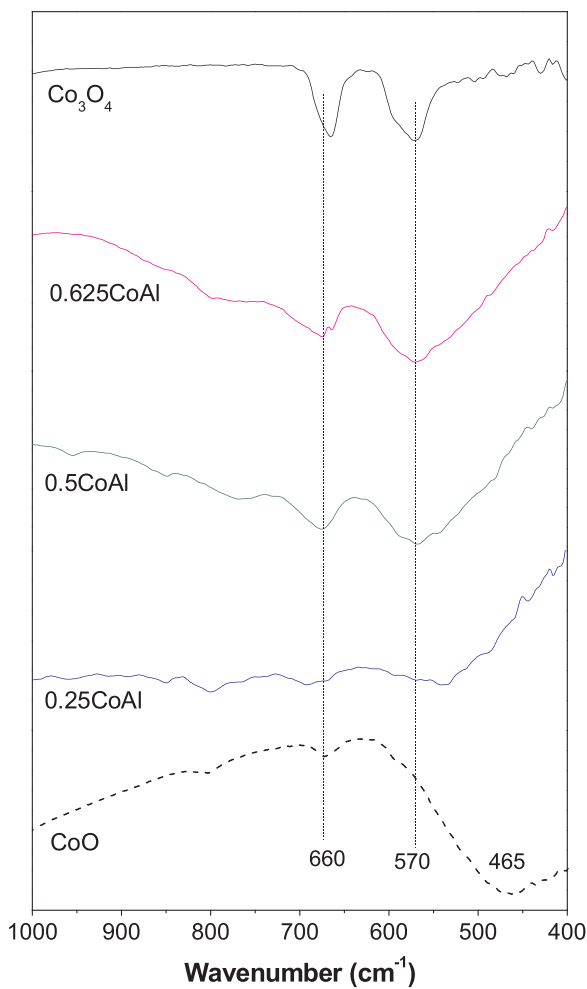


Fig. 5. FTIR spectra from calcined samples.

presence of Co^{2+} in tetrahedral (570 cm^{-1}) and Co^{3+} in octahedral (665 cm^{-1}) coordination [68] were confirmed in sample Co_3O_4 . Sample CoO showed its characteristic broad transmittance band between 400 and 600 cm^{-1} , with a minimum at 465 cm^{-1} [69]. Additional weak band at 660 cm^{-1} was ascribed to Co_3O_4 formed by oxidation of surface CoO . Spectra of XCoAl were significantly attenuated in the 400 – 800 cm^{-1} region, indicating lessening of Co_3O_4 . The sharp bands at around 570 and 660 cm^{-1} , characteristics of the spinel phase [70] became more intense as Co/Al ratio increased.

FTIR spectra of reduced XCoAl samples confirmed the absence of CoO and Co_3O_4 (not shown). As previously shown by XRD data, upon reduction at $600 \text{ }^\circ\text{C}$, only metallic Co and cobalt aluminate coexisted. Moreover, a sort of well defined bands at 3622 , 3529 , and 3460 cm^{-1} were detected for sample 0.25CoAl (Fig. S3A, Supporting information), corresponding to the (OH) stretching vibrations of gibbsite [71].

3.1.6. Surface acidity and basicity

Glycerol aqueous phase reforming can follow different paths, among them, dehydration reactions are involved [72] which are very sensitive to catalysts surface acid-base properties [73]. The acid and basic characteristics of the catalysts were evaluated after reduction at $600 \text{ }^\circ\text{C}$ (Fig. 6) and results are summarized in Table 1. The negligible acidity of sample Co_3O_4 reflects the loss of surface hydroxyls upon reduction. In the case of XCoAl series, surface density of acid sites decreased with Co loading, from $0.784 \text{ mmol}_{\text{NH}_3}/\text{m}^2$ for 0.25CoAl to $0.508 \text{ mmol}_{\text{NH}_3}/\text{m}^2$ for 0.625CoAl . This might be related to the formation of Co_3O_4 and cobalt aluminate species instead of alumina. It should be noted that XRD and FTIR analyses revealed the presence of gibbsite at the lowest

Co/Al (catalyst 0.25CoAl), which is characterized by large amounts of surface hydroxyl groups that favor acidity [61].

The strength of acidic and basic sites was assigned as indicated in Fig. S4 (Supporting information). Overall, the prepared catalysts contain mainly weak and medium acidity (Fig. 6). Lewis type acidity could be expected for the prepared catalysts, as these are characteristic of both γ -alumina [74] and cobalt aluminate [47]. The general trend suggests that Co loading increased the number of weak acid sites, at the expense of intermediate and strong sites, which significantly decreased as Co/Al ratio increased (specially the medium strength site density). This was probably due to the increased presence of cobalt on surface (the number of exposed cobalt atoms increased with Co/Al, Table 1) which would shield the bare alumina.

The density and nature of surface basic sites was studied by CO_2 -TPD (Table 1). $\gamma\text{-Al}_2\text{O}_3$ and Co_3O_4 contained the lowest amount of basic sites. Co_3O_4 hardly adsorbed CO_2 ($14.8 \mu\text{mol}_{\text{CO}_2}/\text{g}$); however, due to its very low surface area ($7.36 \text{ m}^2/\text{g}$), surface density of basic sites amounted $2.01 \mu\text{mol}_{\text{CO}_2}/\text{m}^2$. The surface density of basic sites decreased as Co/Al increased. It is interesting to note the predominance of surface basic functionalities in the prepared XCoAl catalysts, as compared to acid ones (sites density ratio basic/acid is around 4:1) [75]. XCoAl catalysts contain mainly weak basic sites (> 45%), and a small fraction of strong sites (< 22%). Contrarily to acid sites, the formation of medium strength basic sites was favored by the Co/Al ratio.

3.2. Catalytic performance experiments

An aqueous solution of 10 wt.% glycerol (pH 6.6) was fed into the tubular reactor. Data on catalyst performance, in terms of glycerol conversion (X_{Gly}), carbon conversion to gas (X_{gas}) and selectivity to gas (S_{gas}), are shown in Fig. 7. The activity of bare γ -alumina and the homogeneous APR reaction were negligible (not shown) suggesting that neither of them contributed to the activity observed for Co-containing catalysts. In case of γ -alumina, traces of hydroxyacetone were observed at the most severe conditions, owing to its acid property (surface acid sites density $0.55 \mu\text{mol}_{\text{NH}_3}/\text{m}^2$, surface basic sites density $0.17 \mu\text{mol}_{\text{CO}_2}/\text{m}^2$).

At $235 \text{ }^\circ\text{C}/3.5 \text{ MPa}$, the most active catalyst was 0.625CoAl ($X_{\text{Gly}} = 88.4\%$; $X_{\text{gas}} = 21.7\%$). Glycerol conversion decreased as follows: $0.625\text{CoAl} > 0.5\text{CoAl} > 0.25\text{CoAl} > \text{Co}_3\text{O}_4$. Similar order for conversion to gas was observed: $0.625\text{CoAl} > 0.5\text{CoAl} \approx 0.25\text{CoAl} > \text{Co}_3\text{O}_4$. At $260 \text{ }^\circ\text{C}/5.0 \text{ MPa}$, the activity of Co rich catalysts (0.625CoAl , 0.5CoAl , Co_3O_4) increased while performance of catalyst 0.25CoAl hardly varied. S_{gas} varied in the 18–27% range for all the catalysts and both reaction conditions. It seems interesting to note that although the high bulk Co content of catalyst Co_3O_4 , its APR performance was much lower than optimum cobalt-aluminate spinel catalyst. The low number of surface exposed Co^+ atoms of Co_3O_4 (i.e. twenty times lower than 0.625CoAl , Table 1) could be responsible. Moreover, Co_3O_4 showed negligible acidity, which is known to facilitate glycerol conversion through the dehydration mechanism [76]. Indeed, it produced the least amounts of hydroxyacetone, which is formed through the dehydration mechanism [72].

Conversion to gas was below 30% for the prepared catalysts, thus it can be concluded that XCoAl catalysts decomposed glycerol mainly into liquid oxygenated products. High conversion to gas has been related to favorable textural properties [77]. Large surface area would facilitate the adsorption of intermediate molecules onto highly dispersed active phase nanoparticles, facilitating their further conversion into gaseous products. The moderate specific surface area (around $100 \text{ m}^2/\text{g}$) of the prepared catalysts could limit their gasification potential.

It is interesting to note that conversion to gas proportionally increased with the glycerol conversion. That is, the higher the glycerol molecules decomposed, the higher the fraction of C atoms in the feed that were converted into gaseous products. The prepared XCoAl catalysts converted around 24% of the glycerol into gaseous products,

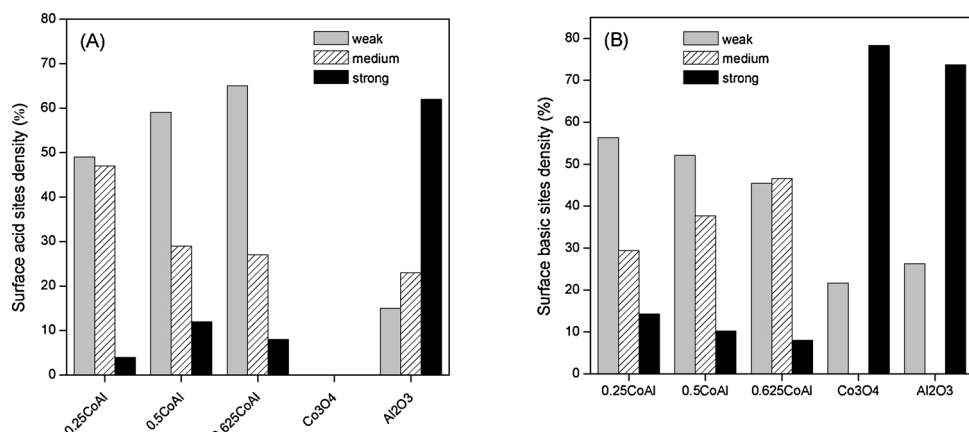


Fig. 6. (A) Surface acid sites density and (B) surface basic sites density.

regardless of the used catalyst and operation conditions (Fig. S6A, Supporting information).

3.2.1. Gaseous products

The main components of the gaseous products were: H₂, CO₂, CH₄, CO and C₂₊ (which includes alkanes and alkenes of two or more carbons). Hydrogen concentration in the gaseous stream varied in the 52–63% and 60–75% ranges, under moderate and severe conditions, respectively (Table 4). The second main product was CO₂ (10–30%), followed by CH₄ (8–14%), CO (0.6–2.3%) and small C₂₊ hydrocarbons (< 6%). Traces of ethane, ethylene, propane, and butane were also detected. The main carbon-containing product was CO₂. Regarding hydrogen selectivity, it varied in the 12–40% and 12–30% under moderate and severe conditions, respectively.

Data in Table 4 revealed that the amount of gas and hydrogen flow produced under both experimental conditions was maximum by catalyst 0.625CoAl (e.g. 322 μmol/g_{cat} min; 168 μmol_{H2}/g_{cat} min at lowest temperature). It is interesting to note that Co-rich catalysts (0.5CoAl, 0.625CoAl and Co₃O₄) were more sensitive to APR operation conditions. This way, the gasification capability and hydrogen production

significantly increased under severe conditions (260 °C/5.0 MPa), while for Co-lean catalysts, the influence of operation conditions was limited.

Catalysts Co₃O₄ gave the highest hydrogen selectivity (S_{H2} = 40.2% and 26.8%, Table 4). Indeed, metal property is known to induce dehydrogenation reactions [78] and catalyst Co₃O₄, with the highest cobalt content, favored dehydrogenation route. In fact, selectivity towards methane was also highest (S_{CH4} = 21.0%), as could be expected from the high methanation activity of Co [79] and the high surface concentration of strong basic sites of sample Co₃O₄, which facilitate methanation [80]. Moreover, methane is the thermodynamically most favored compound under APR conditions, specially under low temperature APR conditions [81]. This would explain the high selectivity to methane measured for Co₃O₄ and also the increase in the H₂/CH₄ ratio by increasing operation temperature observed for these catalysts (Table 4). Acidic sites or media can promote dehydration reactions and undesired Fisher-Tropsch [82], which reduce hydrogen yield in APR. Our results supported that the absence of acidic sites and the abundance of surface basic sites of Co₃O₄ facilitated the dehydrogenation of the glycerol.

Although the high S_{H2}, the glycerol conversion and conversion to

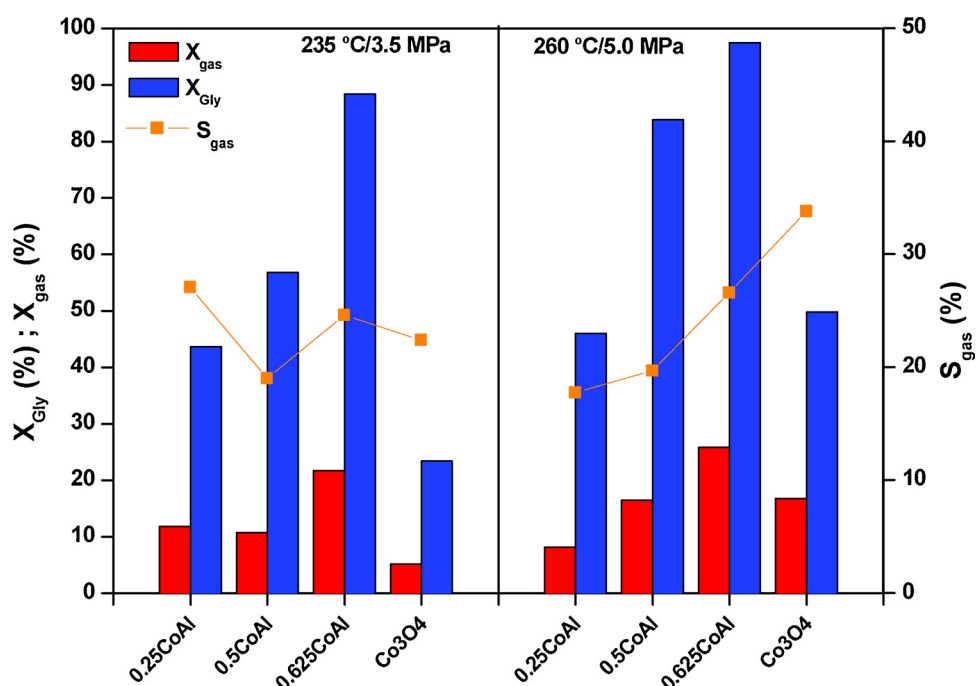


Fig. 7. Effect of Co/Al ratio on glycerol APR activity (conversion to gas and glycerol total conversion) at 235 °C/3.5 MPa and 260 °C/5.0 MPa. Reaction conditions: W_{cat} = 0.5 g, F_{Tot} = 0.2 mL/min, 10 wt.% glycerol/water, WHSV = 24.5 h⁻¹.

Table 4
Glycerol conversion rate and gas products stream characteristics.

Reaction conditions	Catalysts	F_{gas} ($\mu\text{mol/g}_{\text{cat}} \text{ min}$)	F_{H_2} ($\mu\text{mol}_{\text{H}_2}/\text{g}_{\text{cat}} \text{ min}$)	S_{gas} (%)	S_{H_2} (%)	Y_{H_2} (%)	S_{CH_4} (%)	Gaseous products (%)				H_2/CO_2	H_2/CH_4
								H_2	CO_2	CH_4	CO		
235 °C/ 3.5 MPa	0.25CoAl	243	148	27.0	18.0	9.5	5.3	61.0	25.8	7.7	1.4	2.36	7.95
	0.5CoAl	193	105	19.2	11.9	6.8	6.5	54.5	27.6	12.8	0.64	1.98	4.27
	0.625CoAl	322	168	24.6	12.2	10.8	6.0	52.2	30.1	11.1	0.93	1.73	4.71
	Co_3O_4	122	77	22.5	40.2	9.4	21.0	62.6	17.0	14.0	2.3	3.69	4.47
260 °C/ 5.0 MPa	0.25CoAl	224	169	18.0	29.9	10.9	8.1	75.4	9.5	8.8	2.0	7.96	8.57
	0.5CoAl	257	162	19.8	12.5	10.4	4.6	63.0	22.8	10.0	1.8	2.76	6.29
	0.625CoAl	388	231	26.4	15.3	14.9	7.2	59.6	24.9	12.0	0.92	2.39	4.98
	Co_3O_4	323	207	33.3	26.8	13.3	12.4	64.1	17.4	12.7	1.9	3.69	5.06

gas were lowest for sample Co_3O_4 (at 235 °C/3.5 MPa: $X_{\text{Gly}} = 23.4\%$; $X_{\text{gas}} = 5.2\%$) due to its larger Co particle size (Table 3) which conferred the lowest amount of surface Co° atoms, with 1.22×10^{18} atoms/g (Table 1). Catalyst 0.625CoAl, which contained the highest number of exposed Co atoms (23×10^{18} surface Co° atoms/g, Table 1), gave the highest hydrogen yield under both moderate and severe conditions, 10.8% and 14.9%, respectively. The high Co dispersion and the low ratio of acid to basic sites of 0.625CoAl (0.51/1.90) facilitated the initial dehydrogenation of the substrate and somewhat limited the side reactions. It is interesting to note that the CH_4 selectivity decreased from 21% for catalyst Co_3O_4 to 6% for 0.635CoAl, what suggest that the formation of cobalt aluminate spinel also inhibited the methanation activity of cobalt [83].

As previously noted, the production of H_2 (Table 4) increased with operation temperature. However, as conversion increased, the selectivity to hydrogen was compromised (Fig. S6B, Supporting information). Methanation and Fischer-Tropsch reactions take place under similar reaction conditions to APR. Moreover, there is evidence on the similar reaction intermediates [84,85]. Indeed, the observed behavior suggests that cobalt can be active for the above two reactions under APR conditions. If WGS occurred, a ratio H_2/CO_2 of 2.33 could be expected at the APR reactor outlet. However, it was 1.73 for 0.625CoAl what supports H_2 consumption through the above mentioned side reactions.

3.2.2. Liquid products

Product distribution in the condensable phase is shown in Fig. 8A and B. The most abundant liquid product was 1,2-propylene glycol, followed by hydroxyacetone and ethylene glycol. In addition, trace amounts of ethanol, methanol, acetone, acetaldehyde, propionaldehyde, 1-propanol and 2-propanol were also detected for all the catalysts. Overall, there is a clear predominance of oxygenated C_3 compounds as compared to C_2 or C_1 compounds, what would reflect a moderate to weak capability of cobalt aluminate catalysts for direct C–C bond cleavage.

The wide variety in the obtained liquid products confirmed the complexity of the glycerol APR process, where reactions of dehydration, dehydrogenation and hydrogenolysis take place, together with the reforming of the intermediate compounds. Based on the obtained product distribution, a possible reaction pathway for our bifunctional catalysts is depicted in Scheme 1, which comprises two main routes: dehydrogenation to glyceraldehyde (route A), preferably on metal sites, and dehydration to hydroxyacetone (route B), mainly on acid sites. The comparatively higher yield to hydroxyacetone and 1,2-propylene glycol of all the assayed catalysts indicated that the dehydration route was dominant. This can be seen in Fig. 8C, where the ratio between direct dehydration (1,2-propylene glycol and hydroxyacetone) and dehydrogenation (ethylene glycol) products in the liquid phase clearly exceeded unity (varied in 4–10 range). Moreover, a linear correlation was found between this ratio and the density of surface acid sites. It is accepted that hydroxyacetone is formed by elimination of primary

hydroxyl group of glycerol while 3-hydroxypropanal is formed by elimination of the secondary. 3-hydroxypropanal was not detected among the condensable phase products, what implies a higher reactivity of the primary hydroxyl by our catalysts. Also, as previously noted, majority of Lewis sites was expected in these catalysts, which were reported to favor dehydration towards hydroxyacetone rather than to 3-hydroxypropanal [86]. This could explain the absence of the later among the condensable phase products. Also, the very scarce acidity of Co_3O_4 (Table 1), would explain the much lower production of hydroxyacetone and 1,2 propylene glycol by this catalyst.

According to Scheme 1, 1,2-propylene glycol is formed by the hydrogenolysis of hydroxyacetone. Since hydrogen is consumed for the formation of 1,2-propylene glycol, high yield to this by-product could be directly related to a high hydrogenolytic capacity accompanied by limited hydrogen production. However, 0.625CoAl still presented the highest hydrogen yield what reflects that both routes of dehydration/hydrogenolysis and dehydrogenation were present. The moderate concentration of ethylene glycol in liquid products, which is produced from dehydrogenation/decarbonylation of glycerol, would support the above idea. It also points out the high C–C, C–H cleavage activity of catalyst 0.625CoAl, accompanied by an increased production of hydrogen. As previously noted, 0.5CoAl and 0.625CoAl catalysts were characterized by the lowest total acidity but the largest surface density of weak and medium strength acid sites. Indeed, these catalysts led to the formation of moderate amounts of oxygenated hydrocarbons in the liquid phase, what suggests a predominant role of weak and medium strength acid sites (i.e. Lewis sites) in C–O cleavage mechanism rather than strong sites.

For the most active catalyst 0.625CoAl, at 260 °C/5.0 MPa, the yield to hydroxyacetone and 1,2-propylene glycol decreased as compared to that at 235 °C/3.5 MPa (1,2-propylene glycol: 0.37 vs 0.43; hydroxyacetone: 0.11 vs 0.14). This behavior coincided with an important increase in the hydrogen yield of 0.625CoAl with the increase of reaction temperature (Table 4: 10.8% vs. 14.9%) what suggests that dehydrogenation, which competes with dehydration route, was significantly favored under severe conditions. Overall, our experimental results show that catalyst that promote dehydration reactions lead to low hydrogen selectivity as oxygenated intermediates can be hydrogenated to form alkanes.

3.3. Long-term catalytic study

A long-term catalytic run was carried out over the most active catalyst (0.625CoAl) under the so-called severe conditions (at 5.0 MPa/260 °C). Results, shown in Figs. 9 and 10, revealed a significant loss of catalytic performance with reaction time. During the first 3 h of reaction, glycerol conversion remained high, at around 98%, with conversion to gas and selectivity to gas, both showing values of around 30%. Afterwards both X_{Gly} and X_{gas} values gradually decreased. After 30 h of time on stream (TOS), both parameters dropped to 27% and 7%, respectively, while S_{gas} remained around 23%. Consequently, the gas

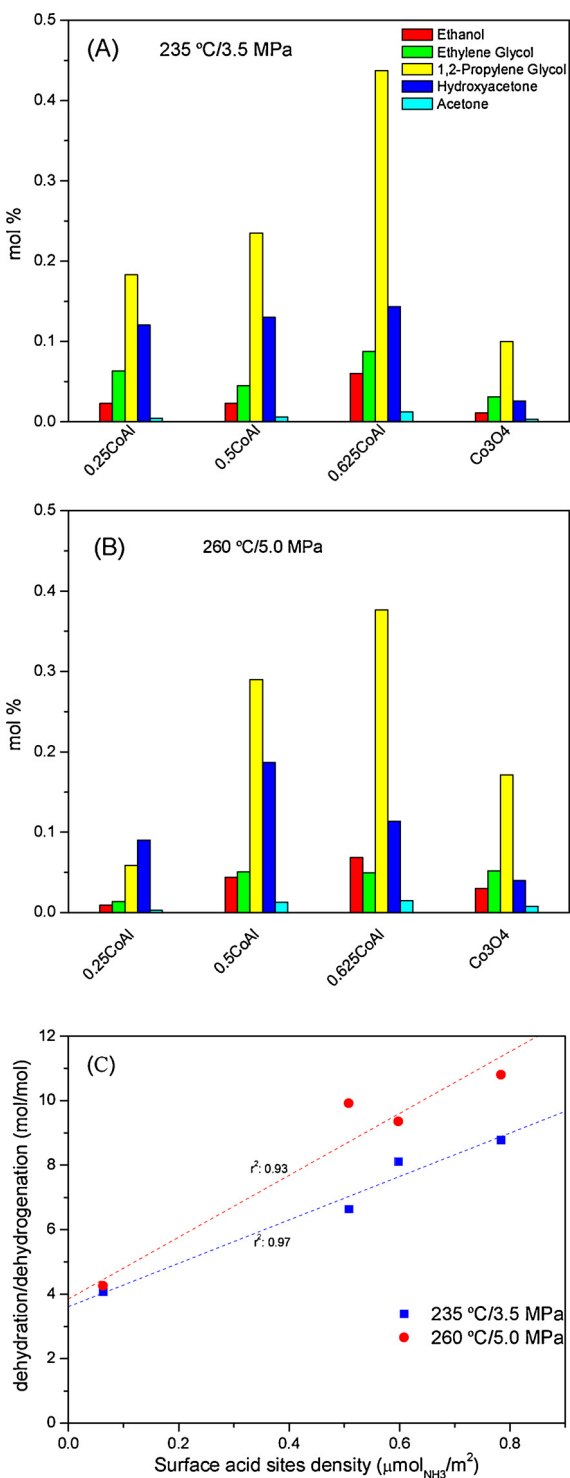


Fig. 8. Liquids products distribution of glycerol APR at 235 °C/3.5 MPa (A) and 260 °C/5.0 MPa (B). Ratio of dehydration to dehydrogenation in the liquid products in function of surface acid sites density (C). Reaction conditions: $W_{\text{cat}} = 0.5 \text{ g}$, $F_{\text{Tot}} = 0.2 \text{ mL/min}$, 10 wt.% glycerol/water, WHSV = 24.5 h⁻¹.

outflow decreased from 11 ml (STP)/min, during the first 3 h, to around 4.7 ml (STP)/min at the end of the test. It is interesting to note that H₂/CO₂ ratio remained very close to the theoretical value (H₂/CO₂ = 2.3) at the initial stages of APR reaction and markedly increased (up to H₂/CO₂ = 12) with TOS, indicating that secondary reactions have taken on a greater role.

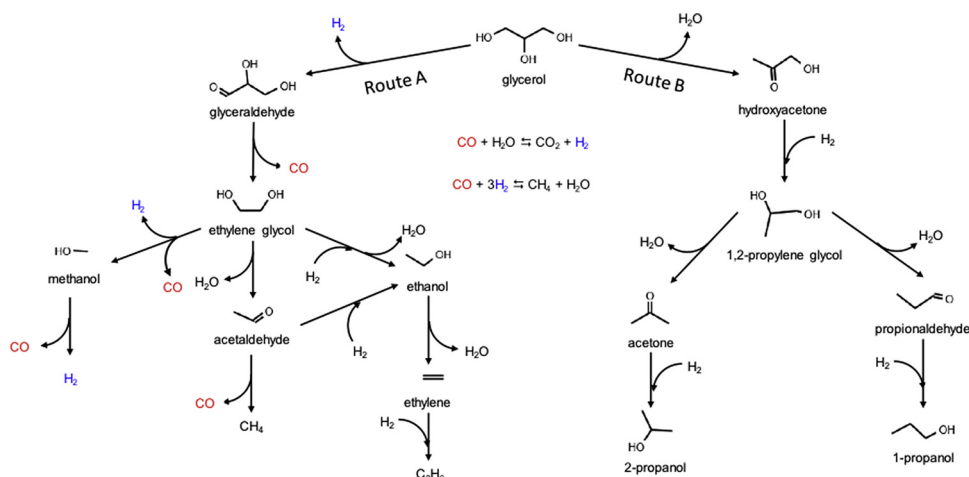
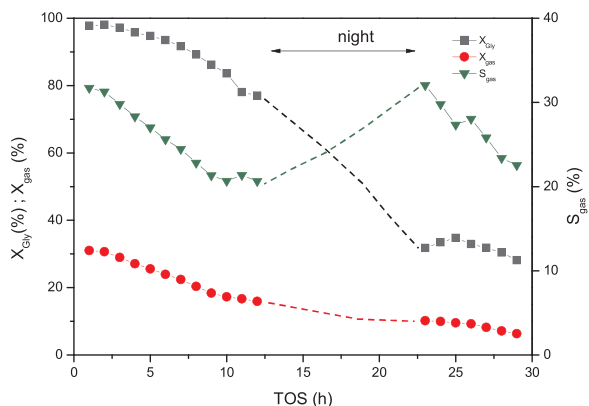
Regarding the condensable phase, 1,2-propylene glycol was the

main species among the liquid products throughout all the reaction period (30 h). It is accepted that hydroxyacetone is produced directly from glycerol through the dehydration route. Subsequent hydrogenation of hydroxyacetone molecule can yield 1,2-propylene glycol [87]. Thus, it suggests that hydroxyacetone was readily hydrogenated over the metallic active sites of 0.625Co/Al catalyst. It was found that concentration of 1,2-propylene glycol and hydroxyacetone, increased during the first hours of reaction (i.e. 1,2-propylene glycol increased up to 38% during the initial 7 h of TOS) and at prolonged TOS, dropped off. Other liquid products such as ethylene glycol, ethanol (dehydrogenation route A in Scheme 1) and acetone (dehydration route B in Scheme 1) progressively declined throughout all reaction period. This behavior reflects that predominant reactions during the initial stages of reaction were different from those measured at prolonged TOS values. It could be interpreted as the hydrogenation reactions (i.e. of hydroxyacetone in Scheme 1) occurring more rapidly than dehydration (i.e. of 1,2-propylene glycol, glycerol) on the acid functionalities on catalyst surface. However, this trend changed as reaction proceeded, and 1,2-propylene glycol dropped off to around 8%. Such a loss of hydrogenation activity was likely caused by the loss of metallic active sites. The intense decrease with TOS of X_{gas} and the continuous downward trend in the ethylene glycol concentration, which is formed through the dehydrogenation route, support the above idea.

It seems interesting to note that dehydrogenation rate (that is C–C and C–H cleavage capacity) was more affected by catalyst deactivation as suggested by the progressive decrease on the levels of ethylene glycol, and its derivate ethanol in the liquid phase. Moreover, the stable profile of hydroxyacetone within all the reaction time, suggests that catalyst still preserved surface acidity. Contrarily, as previously pointed out, 1,2-propylene glycol and hydroxyacetone increased with time during a part of reaction. We hypothesize that this could be due to enhanced acid property on the catalyst surface and oxidation and leaching of cobalt [40]. It has been reported that a part of γ -alumina in the support can be transformed into boehmite as APR reaction proceeds [88]. The surface hydroxyl groups of the later would increase acidity [42], what would drive reaction mechanism towards the dehydration mechanism. The formation of ethylene glycol requires the formation of glyceraldehyde. However, the later was not detected in the liquid stream. It could be due to its rapid decarbonylation to yield ethylene glycol favored by the high C–C cleavage activity of Co [89].

The variability of the gaseous phase composition also evidenced these alterations on the reaction mechanisms. Hydrogen concentration continuously increased throughout the long term APR reaction. C₁ and C₂ gaseous products (i.e. CO, ethylene, ethane), resultant of high C–C cleavage activity, initially increased and at around 12 h of TOS, leveled off (Fig. 10D). Contrarily, methane showed the inverse trend, and decreased with TOS. Considering these dynamic conditions, data collected during the first 12 h of TOS were used to calculate the partial correlation matrix (IBM SPSS Statistics 24) (Pearson coefficients and p values shown in Table S3, Supporting information) and seek for correlations between the formation/consumption of the oxygenated hydrocarbons.

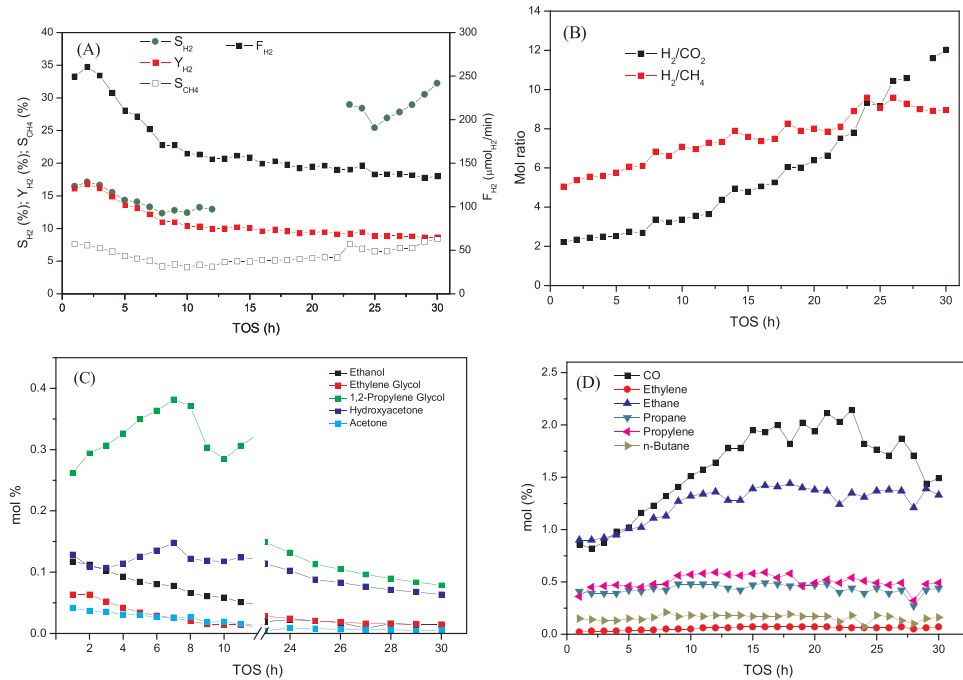
A strong and significant correlation was observed between 1,2-propylene glycol and hydroxyacetone ($r: 0.877$, $p < 0.001$) which supports that both are intermediate products of same decomposition route (i.e. dehydration of glycerol, route B in Scheme 1). There is also an alternative route in which the glycerol molecule undergoes dehydrogenation/decarbonylation (Route A) to yield ethylene glycol. Significant and strong correlation existed between ethylene glycol and ethanol/acetone ($r: 0.984/0.954$, $p < 0.001$) suggesting all of them participate in this reaction chain. Moreover, from Table S3 (Supporting information) it can be observed that correlation between 1,2-propylene glycol, hydroxyacetone and the later species was low and statistically not significant (1,2-propylene glycol $r = 0.274$ and $r = 0.197$; hydroxyacetone $r = 0.495$ and $r = 0.449$ for ethanol and acetone, respectively). This lack of correlation could be interpreted as that both dehydration and dehydrogenation mechanism occurred simultaneously,

**Scheme 1.** Reaction pathways for glycerol APR on XCoAl catalysts.**Fig. 9.** Evolution of X_{Gly} and X_{gas} with TOS for 0.625CoAl catalysts at 260 °C/5.0 MPa. Reaction conditions: $W_{\text{cat}} = 0.5 \text{ g}$, $F_{\text{Tot}} = 0.2 \text{ mL/min}$, 10 wt.% glycerol/water, WHSV = 24.5 h⁻¹.

and independently, in our catalytic system.

Finally, the correlation between liquid products and those in the gas phase was also analyzed. There existed a significant correspondence between levels of the main gaseous products and ethylene glycol, ethanol and acetone in the liquid phase. On the contrary, no correlation existed with respect to hydroxyacetone and 1,2-propylene glycol levels, suggesting that contribution of the dehydration route to production of small gas products was marginal. Indeed, dehydrogenation of glycerol was the main route that produced gas flow.

Regarding the species in the gaseous stream, it is worth pointing out the strong correlation observed between H_2 and CO_2 ($r = -0.988$, $p < 0.001$). The negative value implies the existence of an opposite trend, where selectivity to H_2 increased at the time CO_2 in the gas phase was reduced. This behavior suggests that WGS reaction, which simultaneously produces H_2 and CO_2 , did not pose a relevant role in this catalytic system. The increase with time of CO levels, would support the idea of WGS activity decay of the catalyst. As could be expected, a positive and significant correlation between H_2 and alkanes and alkenes

**Fig. 10.** Evolution with TOS of (A) S_{H_2} , Y_{H_2} , S_{CH_4} and F_{H_2} ; (B) molar H_2/CO_2 and H_2/CH_4 in the gas phase; (C) liquid phase composition; (D) gas phase composition. Data for 0.625CoAl catalysts at 260 °C/5.0 MPa. Reaction conditions: $W_{\text{cat}} = 0.5 \text{ g}$, $F_{\text{Tot}} = 0.2 \text{ mL/min}$, 10 wt.% glycerol/water, WHSV = 24.5 h⁻¹.

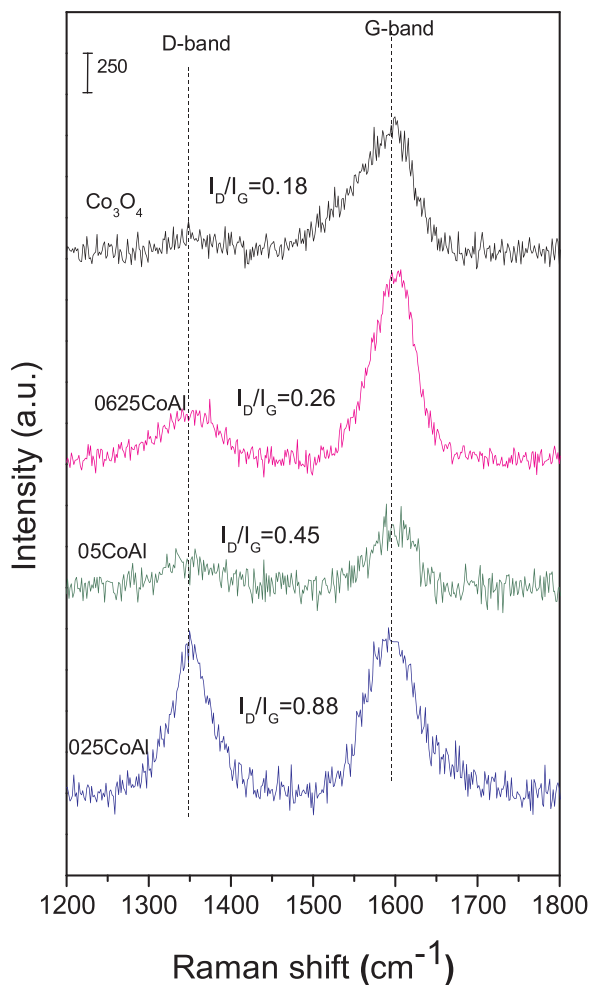


Fig. 11. Raman spectra of spent catalysts.

(ethane, ethylene, propylene) was found as the later are formed through hydrogen reforming reaction of intermediate compounds.

3.4. Characterization of spent catalysts

Spent catalysts discarded from the APR unit ($260\text{ }^{\circ}\text{C}/5.0\text{ MPa}$, TOS: 1 h) were characterized by a sort of techniques. The specific surface area and pore volume notably increased after usage (Table 1), whereas the average pore size decreased (Table S1, Supporting information). Increase in the specific surface area was more pronounced for samples prepared at low Co/Al (S_{BET} increased by 194% for 0.25CoAl, and about 70% for 0.5CoAl and 0.625CoAl samples). On the contrary, specific surface area decreased by around 21% for sample Co_3O_4 . This behavior suggests that aluminium-based compounds could be involved in such a surface area increase (Fig. S7, Supporting information). It is well known that γ -alumina could be hydrated to either boehmite or gibbsite phase under hydrothermal conditions, as hydroxides are thermodynamically more stable than γ -alumina [90]. Moreover, hydration of γ -alumina is enhanced in acidic medium, as occurred in our catalytic system (liquid product stream initial pH: 6.6; final pH: 2.6) due to the presence of soluble oxygenated compounds and dissolved CO_2 . In addition, the aluminium hydroxide can leach from catalysts surface, assisted by acid media [4], which would generate extra porosity in the solid and, thus, increase its specific surface area.

XRD diffraction lines of *fcc* metallic cobalt were observed in all spent catalysts (Fig. 3C). Note that both *fcc* and *hcp* phases were detected in fresh samples what supports the idea of the *fcc* phase being thermodynamically more stable than *hcp* [91]. Sintering notably

increased the cobalt crystallite size of all samples (largest value for Co_3O_4 , with $d_{\text{Co}} = 43\text{ nm}$). It occurred by coarsening of large particles at the expense of smaller ones [92]. This phenomenon has been reported to be favored at high pressures and by the support hydrolysis which breaks the metal-support anchoring [93]. The formation of CoO (PDF 042-1300) and gibbsite was clearly observed for the cobalt aluminate based catalysts. Under hydrothermal conditions, water can act a strong oxidizing agent, even in presence of high hydrogen concentration in the gas stream [42].

H_2 -TPR analysis after reaction are shown in Fig. 2B. Spent Co_3O_4 catalyst showed a single reduction peak, centered at $272\text{ }^{\circ}\text{C}$, which can be ascribed to Co^{88+} species with very weak interaction with the support, product of the re-oxidation of the metallic cobalt [94]. It is known that oxidation of cobalt by water may occur, as anticipated by the low values of the Gibbs free energy [40]. The observed H_2 consumption suggests that around 10% of total cobalt was re-oxidised in this sample. Regarding spent XCoAl catalysts, the amount of easily reducible Co^{88+} species, formed as due to the re-oxidation of metallic cobalt during APR of glycerol [95], was notably lower. For instance, in the case of catalyst 0.625CoAl, it accounted for around 3% of cobalt oxide measured in the fresh sample. For catalyst 0.25CoAl, these species were undetected, probably caused by its limited formation, due to low Co loading and leaching favored by such an acid media.

It seems interesting to note the increased H_2 consumption of spent catalyst at high temperatures (at above $600\text{ }^{\circ}\text{C}$) as compared to fresh samples. Integration of the TPR profile allowed quantifying the cobalt aluminate enrichment at around 31–35% for the exhausted XCoAl catalysts. Moreover, reduction peaks shifted to higher temperatures. We hypothesize that the lessening of surface cobalt species due to leaching, could have limited the spillover phenomena. Also, the observed reduction profile reflects that re-oxidation of metallic cobalt occurred in close contact to aluminum species to form cobalt aluminate. Based on the significant differences in the catalytic performance of Co_3O_4 and XCoAl catalysts, it seems reasonable to assume that alumina species could also have a significant role in the reaction mechanism.

H_2 chemisorption analyses revealed a decrease of around 80–95% in the exposed Co metallic area. Such a significant loss of active sites would imply a sound re-oxidation of Co particles accompanied by leaching. However, the amount of Co leached was not very significant, and remained in the 1.6–3.2% range (Table 1). Moreover, TPR analyses showed that hydrogen consumption of spent catalyst was not reduced to a large degree. In hot-compressed water, where solubility of inorganic oxide materials is low, it can be expected that hydroxylated alumina that leached off can be re-deposited on the catalyst surface [88]. Indeed, this could have diminished the number accessible metallic cobalt atoms. For practical application, regeneration of our catalyst, essentially by a reduction treatment [96], would be required to overcome cobalt re-oxidation.

Deposition of carbonaceous materials onto catalyst surface was investigated by Raman (Fig. 11). Two bands at around $1340\text{--}1400\text{ cm}^{-1}$ and $1540\text{--}1600\text{ cm}^{-1}$ were observed which are related to the defect/amorphous (D-band) and graphite (G-band) modes of carbon, respectively [97]. According to literature, D-band can be associated to non-deactivating carbon, whereas G-band corresponds to deactivating graphitic carbon [98]. In the Raman spectra of the spent catalysts, both D and G bands of the deposited coke at 1340 cm^{-1} and 1604 cm^{-1} , respectively, were clearly observed. This was in agreement with XRD data of spent catalysts which confirmed the formation of graphitic carbon ($2\theta = 26.4^{\circ}$) on 0.25CoAl and 0.5CoAl catalysts. FTIR analysis of the spent 0.625CoAl (after 30 h TOS) also confirmed the presence of coke precursors (Fig. S3B, Supporting information). Raman bands were very broad, which indicates that the coke was highly inhomogeneous in nature. The intensity ratio of D/G ($I_{\text{D}}/I_{\text{G}}$) bands was used to obtain the coke distribution profiles. The fact that $I_{\text{D}}/I_{\text{G}}$ value was in all cases lower than unity (0.18–0.88 range), suggests deposition of mainly graphitic carbon. Moreover, this ratio decreased with Co/Al. This

would also help understanding the observed strong deactivation during the long-term run. As shown in Table 1, density of total surface acid sites decreased with Co/Al, being very low for the reduced Co_3O_4 sample. It could be reasonably hypothesized that carbon deposits were more readily formed during dehydration reactions over the acid sites, with some contribution of metallic cobalt, being the later the unique contribution to carbon deposits on Co_3O_4 . Coke formation in APR occurs to a much lesser extent than in gas phase reforming, due to higher $\text{H}_2\text{O}/\text{carbon}$ and lower operation temperatures. Carbon deposits were detected in our catalysts, probably formed by polymerization of reaction intermediates on acidic sites.

4. Conclusions

Cobalt aluminate spinels were synthetized by coprecipitation at varying Co/Al ratios (XCoAl) and tested for their activity and stability in the aqueous phase reforming of glycerol. Specific surface area of solids was moderate (around $130 \text{ m}^2/\text{g}$), which slightly decreased through reduction at 600°C (to around $100 \text{ m}^2/\text{g}$ for all the samples).

The formation of spinel structure in the XCoAl series was confirmed by XRD, DRS UV-vis and FTIR analyses. Incorporation of aluminium hindered the crystallization of the Co_3O_4 , preventing the formation of large particles. Also, the reduction of cobalt species in the mixed spinel shifted to higher temperatures as compared to the Co_3O_4 alone reflecting an strong Co-O-Al interaction in the mixed spinels. XPS revealed that surface CoAl_2O_4 to Co_3O_4 molar ratio was about 2–3 times larger than bulk composition. Consequently, improved Co dispersion was achieved in the spinel based catalysts, with the maximum number of exposed Co atoms in catalyst 0.625CoAl (ten fold that of Co_3O_4).

Cobalt aluminate system has the potential to display high APR performance if the methanation/Fischer-Tropsch activity can be inhibited. Our catalytic results suggest that XCoAl catalysts maintained the surface basicity of metallic cobalt, while strong acidity of alumina was attenuated. Resultant acid sites were mainly weak and medium strength sites, what inhibits undesired dehydration and other side reactions. Catalyst 0.625CoAl showed the most promising results with high X_{Gly} and X_{gas} and also high hydrogen formation rate ($231 \mu\text{mol}_{\text{H}_2}/\text{g}_{\text{cat}} \text{ min}$ at $260^\circ\text{C}/5.0 \text{ MPa}$). We could conclude that reduction of the Co species on XCoAl catalysts prepared at a Co/Al ratio above the stoichiometric value produced smaller and more stable metallic Co which was more resistant to sintering and coke formation. Remarkable deactivation was reported, which was mainly attributed to sintering and re-oxidation of active phase with some leaching of Co nanoparticles, favored by the acidity of the media, and carbon deposition, mainly on acid sites.

Acknowledgments

The financial support for this work (ENE2016-74850-R) by Mineco and Feder is gratefully acknowledged. A.J. Reynoso would like to thank Dominican Republic MESCYT for his grant. Likewise, the authors thank for technical support provided by SGIker of UPV/EHU and European funding (ERDF and ESF).

Appendix A. Supplementary data

Supplementary material related to this article can be found, in the online version, at doi:<https://doi.org/10.1016/j.apcatb.2018.08.001>.

References

- [1] O.O. James, S. Maity, M.A. Mesubi, K.O. Ogunniran, T.O. Siyanbola, S. Sahu, R. Chaubey, Towards reforming technologies for production of hydrogen exclusively from renewable resources, *Green Chem.* 13 (2013) 2272–2284.
- [2] R. Ciriminna, C. Della Pina, M. Rossi, M. Pagliaro, Understanding the glycerol market, *Eur. J. Lipid Sci. Technol.* 116 (10) (2014) 1432–1439.
- [3] C.H. Zhou, J.N. Beltramini, Y.X. Fan, G.Q. Lu, Chemoselective catalytic conversion of glycerol as a biorenewable source to valuable commodity chemicals, *Chem. Soc. Rev.* 37 (2008) 527–549.
- [4] N.H. Tran, G.S.K. Kannangara, Conversion of glycerol to hydrogen rich gas, *Chem. Soc. Rev.* 42 (2013) 9454–9479.
- [5] Y. Wang, M. Chen, Z. Yang, T. Liang, S. Liu, Z. Zhou, X. Li, Bimetallic Ni-M ($M = \text{Co}, \text{Cu}$ and Zn) supported on attapulgite as catalysts for hydrogen production from glycerol steam reforming, *Appl. Catal. A: Gen.* 550 (2018) 214–227.
- [6] S.J. Yoon, Y.M. Yun, M.W. Seo, Y.K. Kim, H.W. Ra, J.G. Lee, Hydrogen and syngas production from glycerol through microwave plasma gasification, *Int. J. Hydrogen Energy* 38 (34) (2013) 14559–14567.
- [7] M.N.N. Shahirah, J. Gimbut, A. Ideris, M.R. Khan, C.K. Cheng, Catalytic pyrolysis of glycerol into syngas over ceria-promoted $\text{Ni}/\alpha\text{-Al}_2\text{O}_3$ catalyst, *Renew. Energy* 107 (2017) 223–234.
- [8] R. Cortright, R. Davda, J. Dumesic, Hydrogen from catalytic reforming of biomass-derived hydrocarbons in liquid water, *Nature* 418 (6901) (2002) 964–976.
- [9] R.M. Ripken, J. Meuldijk, J.G.E. Gardeniers, S. Le Gac, Influence of the water phase state on the thermodynamics of aqueous-phase reforming for hydrogen production, *ChemSusChem* 10 (24) (2017) 4909–4913.
- [10] I. Coronado, M. Stekrova, M. Reinikainen, P. Simell, L. Lefferts, J. Lehtonen, A review of catalytic aqueous-phase reforming of oxygenated hydrocarbons derived from biorefinery water fractions, *Int. J. Hydrogen Energy* 41 (26) (2016) 11003–11032.
- [11] R.L. Manfro, A.F. da Costa, N.F.P. Ribeiro, M.M.V.M. Souza, Hydrogen production by aqueous-phase reforming of glycerol over nickel catalysts supported on CeO_2 , *Fuel Process. Technol.* 92 (3) (2011) 330–335.
- [12] R.R. Davda, J.W. Shabaker, G.W. Huber, R.D. Cortright, J.A. Dumesic, Aqueous-phase reforming of ethylene glycol on silica-supported metal catalysts, *Appl. Catal. B: Environ.* 43 (1) (2003) 13–26.
- [13] L.I. Godina, A.V. Tokarev, I.L. Simakova, P. Mäki-Arvela, E. Kortesmäki, J. Gläsel, L. Kronberg, B. Etzold, D.Y. Murzin, Aqueous-phase reforming of alcohols with three carbon atoms on carbon-supported Pt, *Catal. Today* 301 (2018) 78–89.
- [14] P. Seretis, P. Tsiaikaras, Aqueous phase reforming (APR) of glycerol over platinum supported on Al_2O_3 catalyst, *Renew. Energy* 85 (2016) 1116–1126.
- [15] S. Larimi, M. Kazemeini, F. Khorasheh, Aqueous phase reforming of glycerol using highly active and stable $\text{Pt}_{0.05}\text{Ce}_x\text{Zr}_{0.95-x}\text{O}_2$ ternary solid solution catalysts, *Appl. Catal. A: Gen.* 523 (2016) 230–240.
- [16] A. Chen, H. Guo, Y. Song, P. Chen, H. Lou, Recyclable $\text{CeO}_2\text{-ZrO}_2$ and $\text{CeO}_2\text{-TiO}_2$ mixed oxides based Pt catalyst for aqueous-phase reforming of the low-boiling fraction of bio-oil, *Int. J. Hydrogen Energy* 42 (15) (2017) 9577–9588.
- [17] I. Esteve-Adell, N. Bakker, A. Primo, E. Hensen, H. García, Oriented Pt nanoparticles supported on few-layers graphene as highly active catalyst for aqueous-phase reforming of ethylene glycol, *ACS Appl. Mater. Interfaces* 8 (49) (2016) 33690–33696.
- [18] M.M. Rahman, T.L. Church, A.I. Minett, A.T. Harris, Effect of CeO_2 addition to Al_2O_3 supports for Pt catalysts on the aqueous-phase reforming of glycerol, *ChemSusChem* 6 (6) (2013) 1006–1013.
- [19] M.C. Kim, T.W. Kim, H.J. Kim, C.U. Kim, J.W. Bae, Aqueous phase reforming of polyols for hydrogen production using supported PtFe bimetallic catalysts, *Renew. Energy* 95 (C) (2016) 396–403.
- [20] L.A. Dosso, C.R. Vera, J.M. Grau, Aqueous phase reforming of polyols from glucose degradation by reaction over Pt/alumina catalysts modified by Ni or Co, *Int. J. Hydrogen Energy* 42 (30) (2017) 18853–18864.
- [21] S. Jeon, Y.M. Park, K. Saravanan, G.Y. Han, B.W. Kim, J.B. Lee, J.W. Bae, Aqueous phase reforming of ethylene glycol over bimetallic platinum-cobalt on ceria-zirconia mixed oxide, *Int. J. Hydrogen Energy* 42 (15) (2017) 9892–9902.
- [22] D.V. Cesari, G.F. Santori, F. Pompeo, M.A. Baldanza, C.A. Henriques, E. Lombardo, M. Schmal, L. Cornaglia, N.N. Nicchio, Hydrogen production from ethylene glycol reforming catalyzed by Ni and Ni-Pt hydrotalcite-derived catalysts, *Int. J. Hydrogen Energy* 41 (47) (2016) 22000–22008.
- [23] A.V. Soares, G. Perez, F.B. Passos, Alumina supported bimetallic Pt-Fe catalysts applied to glycerol hydrogenolysis and aqueous phase reforming, *Appl. Catal. B: Environ.* 185 (2016) 77–87.
- [24] A. Ciftci, D.A.J.M. Ligthart, E.J.M. Hensen, Influence of Pt particle size and Re addition by catalytic reduction on aqueous phase reforming of glycerol for carbon-supported Pt(Re) catalysts, *Appl. Catal. B: Environ.* 174–175 (2015) 126–135.
- [25] D.A. Boga, R. Oord, A.M. Beale, Y.M. Chung, P.C.A. Bruijninx, B.M. Weckhuysen, Highly selective bimetallic Pt-Cu/Mg(Al)O catalysts for the aqueous-phase reforming of glycerol, *ChemCatChem* 52 (2013) 529–537.
- [26] F. Bastan, M. Kazemeini, A.S. Larimi, Aqueous-phase reforming of glycerol for production of alkanes over $\text{Ni}/\text{Ce}_x\text{Zr}_{1-x}\text{O}_2$ nano-catalyst: effects of the support's composition, *Renew. Energy* 108 (C) (2017) 417–424.
- [27] B. Meryemoglu, B. Kaya, S. Irmak, A. Hesenov, O. Erbatur, Comparison of batch aqueous-phase reforming of glycerol and lignocellulosic biomass hydrolysate, *Fuel* 97 (2012) 241–244.
- [28] J.W. Shabaker, G.W. Huber, J.A. Dumesic, Aqueous-phase reforming of oxygenated hydrocarbons over Sn-modified Ni catalysts, *J. Catal.* 222 (1) (2004) 180–191.
- [29] T. Pairojpiriyakul, E. Croiset, W. Kiatkittipong, K. Kiatkittipong, A. Arpornwichanop, S. Assabumrungrat, Hydrogen production from catalytic supercritical water reforming of glycerol with cobalt-based catalysts, *Int. J. Hydrogen Energy* 38 (11) (2013) 4368–4379.
- [30] D.C. Grenoble, M.M. Estadt, D.F. Ollis, The chemistry and catalysis of the water gas shift reaction: 1. The kinetics over supported metal catalysts, *J. Catal.* 67 (1) (1981) 90–102.
- [31] F. Haga, T. Nakajima, H. Miya, S. Mishima, Catalytic properties of supported cobalt catalysts for steam reforming of ethanol, *Catal. Lett.* 48 (3–4) (1997) 223–227.
- [32] J. Llorca, N. Homs, J. Sales, P. Ramírez de la Piscina, Efficient production of

hydrogen over supported cobalt catalysts from ethanol steam reforming, *J. Catal.* 209 (2) (2002) 306–317.

[33] H. Song, L. Zhang, R.B. Watson, D. Braden, U.S. Ozkan, Investigation of bio-ethanol steam reforming over cobalt-based catalysts, *Catal. Today* 129 (3–4) (2007) 346–354.

[34] B. Bayram, I.I. Soykal, D. Deak, J.T. Miller, U.S. Ozkan, Ethanol steam reforming over co-based catalysts: investigation of cobalt coordination environment under reaction conditions, *J. Catal.* 284 (1) (2011) 77–89.

[35] J.S. Moura, M.O.G. Souza, J.D.A. Bellido, E.M. Assaf, M. Opportus, P. Reyes, M.C. Rangel, Ethanol steam reforming over rhodium and cobalt-based catalysts: effect of the support, *Int. J. Hydrogen Energy* 37 (4) (2012) 3213–3224.

[36] B. Zhang, X. Tang, Y. Li, Y. Xu, W. Shen, Hydrogen production from steam reforming of ethanol and glycerol over ceria-supported metal catalysts, *Int. J. Hydrogen Energy* 32 (13) (2007) 2367–2373.

[37] B. Banach, A. Machocki, P. Rybak, A. Denis, W. Grzegorczyk, W. Gac, Selective production of hydrogen by steam reforming of bio-ethanol, *Catal. Today* 176 (1) (2011) 28–35.

[38] S.D. Davidson, J. Sun, Y. Hong, A.M. Karim, A.K. Datye, Y. Wang, The effect of ZnO addition on Co/C catalyst for vapor and aqueous phase reforming of ethanol, *Catal. Today* 233 (2014) 38–45.

[39] G. Wen, Y. Xu, H. Ma, Z. Xu, Z. Tian, Production of hydrogen by aqueous-phase reforming of glycerol, *Int. J. Hydrogen Energy* 33 (22) (2008) 6657–6666.

[40] T. van Haasterecht, C.C.I. Ludding, K.P. de Jong, J.H. Bitter, Stability and activity of carbon nanofiber-supported catalysts in the aqueous phase reforming of ethylene glycol, *J. Energy Chem.* 22 (2) (2013) 257–269.

[41] J. Lee, S.P. Burt, C.A. Carrero, A.C. Alba-Rubio, I. Ro, B.J. O'Neill, H.J. Kim, D.H.K. Jackson, T.F. Kuech, I. Hermans, J.A. Dumesic, G.W. Huber, Stabilizing cobalt catalysts for aqueous-phase reactions by strong metal-support interaction, *J. Catal.* 330 (2015) 19–2.

[42] M. El Doukkali, A. Iriondo, J.F. Cambra, P.L. Arias, Recent improvement on H₂ production by liquid phase reforming of glycerol: catalytic properties and performance, and deactivation studies, *Top. Catal.* 57 (2014) 1066–1077.

[43] Y. Liu, L. Jia, B. Hou, D.K. Sun, D.B. Li, Cobalt aluminate-modified alumina as a carrier for cobalt in Fischer-Tropsch synthesis, *Appl. Catal. A: Gen.* 530 (2017) 30–36.

[44] N.F.P. Ribeiro, R.C.R. Neto, S.F. Moya, M.M.V.M. Souza, M. Schmal, Synthesis of NiAl₂O₄ with high surface area as precursor of Ni nanoparticles for hydrogen production, *Int. J. Hydrogen Energy* 35 (21) (2010) 11725–11732.

[45] Y.J. Wong, M.K. Koh, M. Khavarian, A.R. Mohamed, Investigation on cobalt aluminate as an oxygen carrier catalyst for dry reforming of methane, *Int. J. Hydrogen Energy* 42 (47) (2017) 28363–28376.

[46] S. Gündüz, T. Dogu, Hydrogen by steam reforming of ethanol over Co-Mg incorporated novel mesoporous alumina catalysts in tubular and microwave reactors, *Appl. Catal. B: Environ.* 168–169 (2015) 497–508.

[47] B. Hu, W.G. Kim, T.P. Sulmonetti, M.L. Sarazen, S. Tan, J. So, Y. Liu, R.S. Dixit, S. Nair, C.W. Jones, A mesoporous cobalt aluminate spinel catalyst for nonoxidative propane dehydrogenation, *ChemCatChem* 9 (17) (2017) 3330–3337.

[48] R.C. Reuel, C.H. Bartholomew, The stoichiometries of H₂ and CO adsorptions on cobalt: effects of support and preparation, *J. Catal.* 85 (1) (1984) 63–77.

[49] B. Jongsomjit, J.G. Goodwin, Co-support compound formation in Co/Al₂O₃ catalysts: effect of reduction gas containing CO, *Catal. Today* 77 (2002) 191–204.

[50] Z. Skoufa, G. Xantri, E. Heracleous, A.A. Lemonidou, A study of Ni-Al-O mixed oxides as catalysts for the oxidative conversion of ethane to ethylene, *Appl. Catal. A: Gen.* 471 (2014) 107–117.

[51] C. Otero-Areán, M. Peñarroya-Mentruit, E. Escalona-Platero, F.X. Llabrés i Xamena, J.B. Parra, Sol-gel method for preparing high surface area CoAl₂O₄ and Al₂O₃-CoAl₂O₄ spinels, *Mater. Lett.* 39 (1999) 22–27.

[52] G. Li, L. Hu, J.M. Hill, Comparison of reducibility and stability of alumina-supported Ni catalysts prepared by impregnation and co-precipitation, *Appl. Catal. A: Gen.* 301 (1) (2006) 16–24.

[53] C.H. Bartholomew, Mechanisms of catalyst deactivation, *Appl. Catal. A: Gen.* 212 (1–2) (2001) 17–60.

[54] M.G. Musolino, C. Busacca, F. Mauriello, R. Pietropaolo, Aliphatic carbonyl reduction promoted by palladium catalysts under mild conditions, *Appl. Catal. A: Gen.* 379 (1–2) (2010) 77–86.

[55] Y. Ji, Z. Zhao, A. Duan, G. Jiang, J. Liu, Comparative study on the formation and reduction of bulk and Al₂O₃-supported cobalt oxides by H₂-TPR technique, *J. Phys. Chem. C* 113 (2009) 7186–7199.

[56] H.H. Kung, Catalytic behavior of a cation in a solid solution-an electrostatic potential approach, *J. Catal.* 73 (1982) 387–395.

[57] B. Jongsomjit, J. Panpranot, J.G. Goodwin, Co-support compound formation in alumina-supported cobalt catalysts, *J. Catal.* 204 (2001) 98–109.

[58] N. Srisawad, W. Chaitree, O. Mekasuwanumrong, P. Praserthdam, J. Panpranot, Formation of CoAl₂O₄ nanoparticles via low-temperature solid-state reaction of fine gibbsite and cobalt precursor, *J. Nanomater.* 2012 (2012) 108369–8.

[59] K. Srinivasan, C.S. Swamy, Catalytic decomposition of nitrous oxide over calcined cobalt aluminum hydrotalcite, *Catal. Today* 53 (4) (1999) 725–737.

[60] A.E. Ray, S.R. Smith, J.D. Scofield, Study of the phase transformation of cobalt, *J. Phase Equilib.* 12 (6) (1991) 644–647.

[61] X. Yang, Z. Sun, D. Wang, W. Forsling, Surface acid-base properties and hydration/dehydration mechanisms of aluminum (hydr)oxides, *J. Colloid Interface Sci.* 308 (2007) 395–404.

[62] Y. Liu, L. Jia, B. Hou, D. Sun, D. Li, Cobalt aluminate-modified alumina as a carrier for cobalt in Fischer-Tropsch synthesis, *Appl. Catal. A: Gen.* 530 (2017) 30–36.

[63] Y. Brik, M. Kacimi, M. Ziyad, F. Bozon-Verdúraz, Titania-supported cobalt and cobalt-phosphorus catalysts: characterization and performances in ethane oxidative dehydrogenation, *J. Catal.* 202 (2001) 118–128.

[64] J. Vakros, C. Kordulis, A. Lycurghiotsis, Cobalt oxide supported γ -alumina catalyst with very high active surface area prepared by equilibrium deposition filtration, *Langmuir* 18 (2) (2002) 417–422.

[65] D.L. Wood, J.P. Remeika, Optical absorption of tetrahedral Co³⁺ and Co²⁺ in garnets, *J. Chem. Phys.* 46 (1967) 3595.

[66] A. Sarellas, D. Niakolas, K. Bourikas, J. Vakros, C. Kordulis, The influence of the preparation method and the Co loading on the structure and activity of cobalt oxide/ γ -alumina catalysts for NO reduction by propene, *J. Colloid Interface Sci.* 295 (2006) 165–172.

[67] O.O. James, S. Maity, Temperature programmed reduction (TPR) studies of cobalt phases in γ -alumina supported cobalt catalyst, *J. Pet. Technol. Altern. Fuels* 7 (1) (2016) 1–12.

[68] L.H. Ai, J. Jiang, Rapid synthesis of nanocrystalline Co₃O₄ by a microwave-assisted combustion method, *Powder Technol.* 195 (1) (2009) 11–14.

[69] C.W. Tang, C.B. Wang, S.H. Chien, Characterization of cobalt oxides studied by FT-IR, Raman, TPR and TG-MS, *Thermochim. Acta* 473 (2008) 68–73.

[70] I. Mindru, G. Marinescu, D. Gingas, L. Patron, C. Ghica, M. Giurcină, Blue CoAl₂O₄ spinel via complexation method, *Mater. Chem. Phys.* 122 (2–3) (2010) 491–497.

[71] T.C. Alex, R. Kumar, S.K. Roy, S.P. Mehrotra, Mechanically induced reactivity of gibbsite: part 2. Attrition milling, *Powder Technol.* 264 (2014) 229–235.

[72] J. Remón, J.R. Giménez, A. Valiente, L. García, J. Arauzo, Production of gaseous and liquid chemicals by aqueous phase reforming of crude glycerol: influence of operating conditions on the process, *Energy Convers. Manage.* 110 (2016) 90–112.

[73] R. Estevez, S. Lopez-Pedrajas, F. Blanco-Bonilla, D. Luna, F.M. Bautista, Production of acrolein from glycerol in liquid phase on heterogeneous catalysts, *Chem. Eng.* 282 (2015) 179–186.

[74] J. Lif, I. Odenbrand, M. Skoglundh, Sintering of alumina-supported nickel particles under amination conditions: support effects, *Appl. Catal. A: Gen.* 317 (1) (2007) 62–69.

[75] C. Azer, A.R. Ramadan, G. Ghaly, J. Ragai, Preparation and characterization of cobalt aluminate spinels CoAl₂O₄ doped with magnesium oxide, *Adsorp. Sci. Technol.* 30 (5) (2012) 399–407.

[76] H. Park, Y.S. Yun, T.Y. Kim, K.R. Lee, J. Baek, J. Yi, Kinetics of the dehydration of glycerol over acid catalysts with an investigation of deactivation mechanism by coke, *Appl. Catal. B: Environ.* 176–177 (2015) 1–10.

[77] M. El Doukkali, A. Iriondo, P.L. Arias, J. Reques, I. Gandarias, L. Jalowiecki-Duhamel, F. Dumeignil, A comparison of sol-gel and impregnated Pt/or and Ni based γ -alumina catalysts for bioglycerol aqueous phase reforming, *Appl. Catal. B: Environ.* 125 (2012) 516–529.

[78] B. Liu, F. Gao, Navigating glycerol conversion roadmap and heterogeneous catalyst selection aided by density functional theory: a review, *Catalysts* 8 (2) (2018) 44–71.

[79] M.A. Vannice, The catalytic synthesis of hydrocarbons from H₂O/CO mixtures over the group VIII metals: I. The specific activities and product distributions of supported metals, *J. Catal.* 37 (1975) 449–461.

[80] K. Stangeland, D. Kalai, H. Li, Z. Yu, CO₂ methanation: the effect of catalysts and reaction conditions, *Energy Procedia* 105 (2017) 2022–2027.

[81] R.R. Davda, J.W. Shabaker, G.W. Huber, R.D. Cortright, J.A. Dumesic, A review of catalytic issues and process conditions for renewable hydrogen and alkanes by aqueous-phase reforming of oxygenated hydrocarbons over supported metal catalysts, *Appl. Catal. B: Environ.* 56 (1–2) (2005) 171–186.

[82] R.R. Davda, J.A. Dumesic, Renewable hydrogen by aqueous-phase reforming of glucose, *Chem. Commun.* 0 (2004) 36–37.

[83] D.J. Moodley, A.M. Saib, J. van de Loosdrecht, C.A. Welker-Nieuwoudt, B.H. Sigwela, J.W. Niemantsverdriet, The impact of cobalt aluminate formation on the deactivation of cobalt-based Fischer-Tropsch synthesis catalysts, *Catal. Today* 171 (1) (2011) 192–200.

[84] A. Kirilin, A. Tokarev, E. Murzina, L. Kustov, J.P. Mikkola, D. Murzin, Reaction products and transformations of intermediates in the aqueous-phase reforming of sorbitol, *ChemSusChem* 3 (2010) 708–718.

[85] V. Sánchez-Escribano, M.A.L. Vargas, E. Finocchio, G. Busca, On the mechanisms and the selectivity determining steps in syngas conversion over supported metal catalysts: an IR study, *Appl. Catal. A: Gen.* 316 (2007) 68–74.

[86] A. Alhanash, E.F. Kozhevnikova, I.V. Kozhevnikov, Gas-phase dehydration of glycerol to acrolein catalysed by caesium heteropoly salt, *Appl. Catal. A: Gen.* 378 (2010) 11–18.

[87] E.P. Maris, R.J. Davis, Hydrogenolysis of glycerol over carbon-supported Ru and Pt catalysts, *J. Catal.* 249 (2) (2007) 328–337.

[88] D.J.M. de Vlieger, B.L. Mojet, L. Lefferts, K. Seshan, Aqueous phase reforming of ethylene glycol – role of intermediates in catalyst performance, *J. Catal.* 292 (2012) 239–245.

[89] D. Sun, Y. Yamada, S. Sato, W. Ueda, Review glycerol hydrogenolysis into useful C3 chemicals, *Appl. Catal. B: Environ.* 193 (2016) 75–92.

[90] G. Lefèvre, M. Duc, P. Lepeut, R. Caplain, M. Féodoroff, Hydration of γ -alumina in water and its effects on surface reactivity, *Langmuir* 18 (20) (2002) 7530–7537.

[91] O. Kitakami, H. Sato, Y. Shimada, F. Sato, M. Tanaka, Size effect on the crystal phase of cobalt fine particles, *Phys. Rev. B* 56 (21) (1997) 13849–13854.

[92] T. van Haasterecht, C.C.I. Ludding, K.P. de Jong, J.H. Bitter, Toward stable nickel catalysts for aqueous phase reforming of biomass-derived feedstock under reducing and alkaline conditions, *J. Catal.* 319 (2014) 27–35.

[93] W.C. Ketchie, E.P. Maris, R.J. Davis, In-situ X-ray absorption spectroscopy of supported Ru catalysts in the aqueous phase, *Chem. Mater.* 19 (14) (2007) 3406–3411.

[94] P.J. van Berge, J. van de Loosdrecht, S. Barradas, A.M. van der Kraan, Oxidation of cobalt based Fischer-Tropsch catalysts as a deactivation mechanism, *Catal. Today* 58 (4) (2000) 321–334.

[95] G. Wen, Y. Xu, H. Ma, Z. Xu, Z. Tian, Production of hydrogen by aqueous-phase reforming of glycerol, *Int. J. Hydrogen Energy* 33 (22) (2008) 6657–6666.

[96] A.V. Kirilin, A.V. Tokarev, L.M. Kustov, T. Salmi, J.P. Mikkola, D.Y. Murzin, Aqueous phase reforming of xylitol and sorbitol: comparison and influence of substrate structure, *Appl. Catal. A: Gen.* 435–436 (2012) 172–180.

[97] F.F. de Sousa, H.S.A. de Sousa, A.C. Oliveira, M.C.C. Junior, A.P. Ayala, E.B. Barros, B.C. Viana, J.M. Filho, A.C. Oliveira, Nanostructured Ni-containing spinel oxides for the dry reforming of methane: effect of the presence of cobalt and nickel on the deactivation behaviour of catalysts, *Int. J. Hydrogen Energy* 37 (2012) 3201–3212.

[98] B.C. Miranda, R.J. Chimentão, J.B.O. Santos, F. Gispert-Guirado, J. Llorca, F. Medina, F. López Bonillo, J.E. Sueiras, Conversion of glycerol over 10%Ni/-Al₂O₃ catalyst, *Appl. Catal. B: Environ.* 147 (2014) 464–480.